Crystallography and elastic anisotropy in fatigue crack nucleation at nickel alloy twin boundaries

Xiaoxian Zhang [a, *], Jean Charles Stinville [b], Tresa M. Pollock [b], Fionn P.E. Dunne [a]

[a] Department of Materials, Imperial College London, London, UK

[b] Materials Department, University of California Santa Barbara, Santa Barbara, USA

[*] Corresponding author, E-mail address: xiaoxian.zhang18@imperial.ac.uk

Abstract

Fatigue crack nucleation at annealing twin boundaries (TBs) within polycrystal nickel-based superalloy $René\,88DT$ is investigated with a microstructure-sensitive crystal plasticity (CP) model, digital image correlation strain measurements and experimental SEM crack nucleation observations. Strong slip localizations at TBs were experimentally observed and predicted by the CP model, which also showed high predicted geometrically necessary dislocation and corresponding stored energy densities, capturing experimental observations of crack nucleation. A systematic study of elastic anisotropy was found to drive local elastic constraint and hence resolved shear stress, slip activation, GND density and stored energy density, demonstrating for this reason that TBs are preferential sites for crack nucleation in this alloy. The parent grain / twin pair crystallographic orientation with respect to remote loading was also demonstrated to be key to slip activation parallel to TBs and hence to stored energy density and fatigue crack nucleation, and the range of most damaging parent grain orientations has been identified.

1. Introduction

Crack nucleation is a key aspect of fatigue fracture in metal alloys and is preceded by irreversible slip and strain localization, as commonly observed in experiments. Dislocation structures form as a result of the forward and backward cyclic loading, observed as persistent slip bands (PSBs) with distinctive structures [1]. Sauzay et al. have assessed the role of PSBs in fatigue crack nucleation in some detail [2][3]. Mura et al. [4][5] investigated the driving forces for fatigue crack nucleation and suggested a theory based on strain energy, in which dislocation dipoles are annihilated to form a micro-void (crack) when the stored elastic strain energy reaches a critical value. A related theory was developed by Dunne et al. at the mesoscale which considers the elastic energy stored by lattice curvature, and hence related to geometrically necessary dislocation density, which has been coupled with crystal plasticity finite element (CPFE) methods to predict microstructure-sensitive fatigue crack nucleation sites, and shows good agreement with experiments [6][7][8].

Annealing twin boundaries are well known to be preferential fatigue crack nucleation sites in polycrystal alloys with low stacking fault energy [9][10]. Neumann et al. argue that this phenomenon is caused by the elastic incompatibility stress, which facilities slip at the twin boundary (TB), and subsequently triggers fatigue crack nucleation. Fatigue cracks at TBs are always linked with slip localization [11][12]. Stinville et al. investigated two typical slip configurations at TBs using high resolution digital image correlation (HR-DIC) strain measurement techniques, and showed that

parallel slip systems play an important role in plastic strain localization and slip irreversibility [10][13]. In addition, a statistical study showed three key factors (global/nominal Schmid factor, elastic anisotropy and TB length) contributed to the probability of fatigue crack nucleation at TBs [12]. In addition, Li et al. argued the fatigue crack mechanism depends on the local stress state [14][15].

Wei et al. used a 3D discrete dislocation modelling approach to investigate the hardening effect of TBs which was found to be minimised when the loading axis is arranged to be 45^{o} to the TB; for this configuration, dislocation glide along the slip plane parallel to the TB was found to occur without strong resistance [16]. Sangid et al. used molecular dynamics to calculate the energy required for dislocation penetration through a TB, and showed that $\Sigma 3$ boundaries have the highest values compared with other grain-boundary types [17][18]. Recently, high elastic strain gradients local to TBs have been observed using dark-field X-ray diffraction characterization [19]. More recently in an integrated experimental and computational investigation, it has been demonstrated that elastic strain localization at TBs is strongly dependent on the crystal elastic anisotropy and morphology of the grains at the TB, but less so on the neighboring grains [20]. Hence the local stress state, which drives slip activation and is strongly influenced by elastic anisotropy and grain boundary constraint, together with highly anisotropic slip, are key factors in fatigue crack nucleation at TBs.

This paper investigates the mechanistic link between crystallographic orientation (and corresponding elastic anisotropy) of annealing twins at TBs and the local stored

energy density in order to establish cause and effect for observed fatigue crack nucleation at TBs. While the role of dislocation density on stored energy is recognized, we do not include explicit representation of discrete dislocation events (for example, through interactions with twin [16] and grain boundaries [17][18]), which other researchers have addressed. Rather, crystal plasticity modelling studies are integrated with experimental HR-DIC strain measurement local to TBs by generating faithfully-representative model microstructures from quantitative characterization of sample microstructures. With the model established, systematic studies of crystal elastic anisotropy (Zener coefficient) and twin crystallographic orientation on local stored energy densities, and their relationship to observed crack nucleation events, are presented to understand the mechanistic basis of twins in nickel alloy fatigue crack nucleation.

2. Methods

2.1 Material, fatigue test and SEM, EBSD and HR-DIC characterization

Polycrystal nickel-based superalloy $René\ 88DT$ produced by powder metallurgy is used in this study. This alloy has nominal chemical composition: 13%Co, 16%Cr, 4%Mo, 4%W, 2.1%Al, 3.7%Ti, 0.7%Nb, 0.03%C, 0.015%B (wt%). There are two precipitate phases in the matrix of this alloy, namely a secondary γ' with a 100 nm averaged size and tertiary γ' with a 10 nm averaged size. Both are coherent with the FCC γ matrix. A large population of annealing twins can be observed from the 2D EBSD cross-section map shown in Fig. 1(a). This alloy has a 0.2% yield strength of 1080MPa and Young's

modulus of 217GPa in monotonic tensile testing. Fatigue tests were performed in an air, room temperature environment with uniaxial symmetric push-pull loading under stress control with R-ratio of -1, frequency 1Hz, and the maximum applied stress of 1140MPa. Cylindrical dog-bone samples were employed with two parallel flat areas of 2.5mm x 8mm forming the sample gauge which is machined in to the cylindrical sample of diameter 6mm. More details can be found in [21].

Prior to fatigue testing, samples were processed by SiC papers and chemo-mechanically polished. Before deformation, reference EBSD maps were obtained with an EDAX OIM-Hikari XM4 EBSD detector, with scanning step size 0.8μm. During the fatigue testing, cyclic loading was interrupted after the 1st half cycle, 1st full cycle, 400th and 5000th cycles, and corresponding SEM and HR-DIC characterizations were performed during these interruptions as shown in Fig. 1(b). More details on the low cycle fatigue behavior of the investigated alloy are presented elsewhere [13].

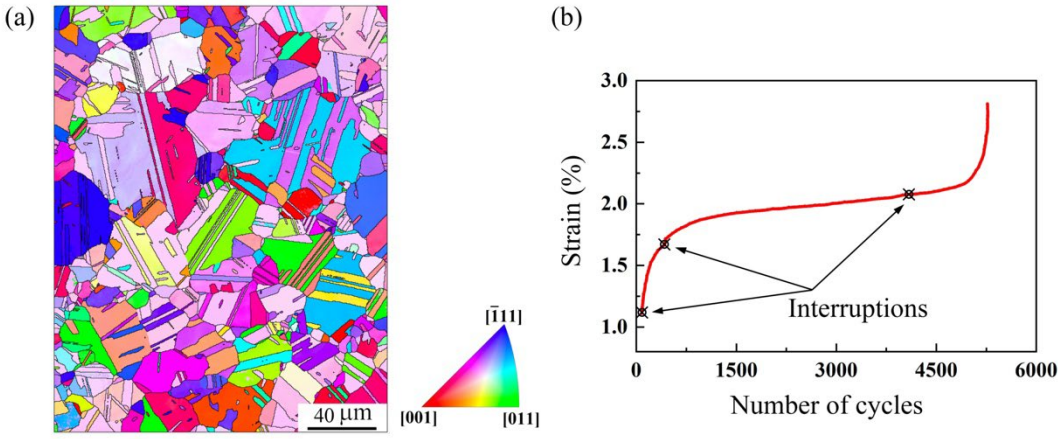

Figure 1. (a) EBSD map of a region contains a large number of annealing twin boundaries of *René 88DT*; (b) Macroscopic strain evolution during cyclic loading [13];

HR-DIC maps were obtained with horizontal field width of 138 μm, with spatial resolution of ~101 nm. The Heaviside-DIC method is used to quantitatively characterize the local displacement induced by slip. This method integrates a jump/step vector by the use of a Heaviside function in the conventional DIC shape function for measurements of discontinuous displacements [13]. The resulting maps display the local in-plane slip amplitude at the scale of nanometers that corresponds to the in-plane displacement induced along slip events. Previous studies indicate a sensitivity of ~10 nm and a displacement resolution of few nanometer [13]. EBSD and HR-DIC maps are merged using distortion and data merging algorithms [13].

2.2 Computational crystal plasticity methodology

Microstructure-faithful finite element models were constructed based on the crystallographic orientation and morphological information obtained from the EBSD scan in Fig. 1(a), such that the finite twin thicknesses along with the parent/twin crystal orientation relationship (twist 60° along their common <111>) have been considered in the CPFE modelling.

The sub-model was developed using ~140,000 three-dimensional C3D20R elements shown in Fig. 2(a). The average element size is ~ 1.2 μm, relative to an average grain size of 20 μm. While discrete slip traces can't be explicitly predicted by CPFE due to its continuum nature. This paper aims to use CPFE to predict the local intragranular plastic field at the TBs but not seek explicit comparison with Heaviside DIC slip trace analysis.

The grains, and their crystallographic orientations, were assumed to be prismatic through a small thickness normal to the free surface, in the absence of data on sub-surface microstructure. Previous work [6][22] has shown this 2.5D (extrusion) assumption can affect the predicted surface plastic strains. To minimize this effect, the particular ROI selected is shown to give good agreement between model and experimentally observed slip activation, as discussed in Section 3 (with respect to Figure 7). In addition, in order to ensure that the computational results on the free surface show limited dependence on (z-direction) thickness, a sensitivity analysis has been conducted and is included in Appendix 1, which demonstrates the effect of the model thickness is not strong for the microstructure shown in figure 2.

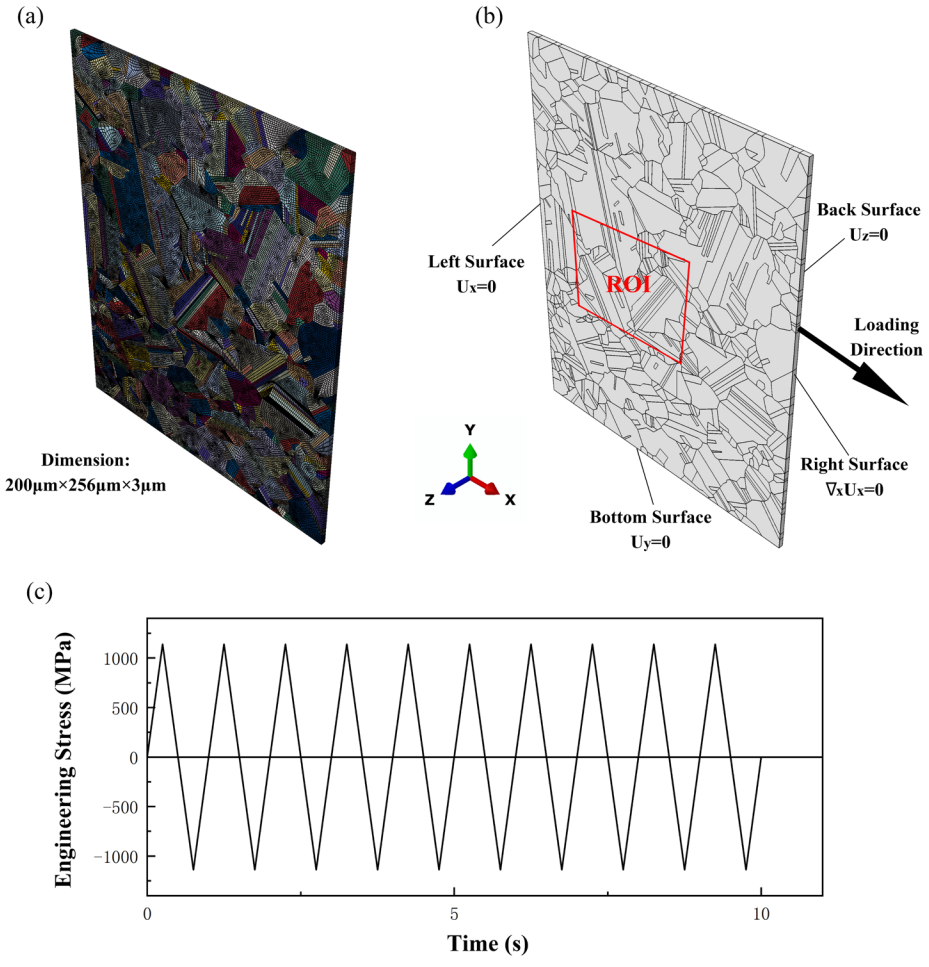

Figure 2. (a) Finite element sub-model reconstructed from EBSD scans; (b) Loading boundary condition and region of interest (ROI); (c) The applied cyclic loading (shown for 10 cycles)

To represent the stress state in the uniaxial push-pull mode experiments, boundary and loading conditions were imposed on the model microstructure as shown in Fig. 2(b). Uniaxial stress control loading was imposed on the right surface, such that the averaged peak xx-stress on this surface was 1140MPa reflecting that applied in the experiments. The right, loaded surface was constrained to remain planar during the loading and other boundary conditions applied were as shown in the figure. Note that all the TB regions of interest (ROI) within the microstructure were chosen to be well removed from the boundaries to eliminate far field effects as shown by the red rectangle in Fig. 2(b). The corresponding loading history is plotted in Fig. 2(c). While only ten cycles of loading are modelled, it has been established both experimentally and in CP polycrystal modelling that the strongest evolution of key microstructural quantities occurs within the first few loading cycles which is then typically followed by a stable (and slow) cyclic rate of increase. Hence modelling over ten cycles gives good insight into the role of critical features of the microstructure (such as twin boundaries) compared to other (non-critical) regions.

A gradient enhanced crystal plasticity model coupled with elastic anisotropy is

utilized for the nickel crystal behaviour. The plastic velocity gradient $\boldsymbol{L_p}$ is given in terms of slip directions and plane normals by

$$\boldsymbol{L_p} = \sum_{i=1}^{12} \dot{\gamma}^i \, \boldsymbol{s}^i \otimes \boldsymbol{n}^i \tag{5}$$

where $\boldsymbol{s}^i$ is the slip direction, and $\boldsymbol{n}^i$ the plane normal of the i^{th} slip system. $\dot{\gamma}^i$ is slip rate, which is determined based on thermally activated dislocation escape and glide [23][24] from

$$\dot{\gamma}^i = \rho_{SSD}^m b^2 \nu \exp\left(-\frac{\Delta F}{kT}\right) \sinh\left(\frac{\left|\tau^i - \tau_C^i\right| \Delta V}{kT}\right) \tag{6}$$

where ρ_{SSD}^m is the density of mobile dislocations, b the Burgers vector, and ν the frequency of attempts of dislocations to jump the energy barrier; ΔF is the activation energy and ΔV the corresponding volume. k is the Boltzmann constant and T the temperature. τ^i is the resolved shear stress on the i^{th} slip system, and τ_C^i the slip strength, which is updated with accumulated slip following an dislocation based hardening law

$$\tau_C = \tau_0 + \alpha G b \sqrt{\rho_{SSD}^s + \rho_{GND}} \tag{7}$$

where τ_0 is the initial slip strength without strain hardening, G the shear modulus, α the Taylor hardening coefficient. Note that the slip system critical resolved shear stress (CRSS) is therefore the slip strength (as defined above) plus any contribution which comes from thermally activated events as reflected in eqn (6). The density of sessile statistically stored dislocations ρ_{SSD}^s is determined from the isotropic hardening law

$$\dot{\rho}_{SSD}^s = \lambda \dot{p} \tag{8}$$

where λ is a hardening coefficient, and p the effective plastic strain, defined as

$$p = \left(\frac{2}{3}\boldsymbol{\varepsilon}^{\mathrm{p}} : \boldsymbol{\varepsilon}^{\mathrm{p}}\right)^{\frac{1}{2}} = \left[\frac{2}{3}\left((\varepsilon_{xx}^p)^2 + (\varepsilon_{yy}^p)^2 + (\varepsilon_{zz}^p)^2 + 2(\varepsilon_{xy}^p)^2 + 2(\varepsilon_{yz}^p)^2 + 2(\varepsilon_{xz}^p)^2\right)\right]^{\frac{1}{2}} \tag{9}$$

The SSD hardening behaviour described by eqn (8) would normally be anticipated to include a recovery term but in the alloy considered, the average polycrystal stress-strain response (see later) shows really rather little isotropic hardening. This results in very low SSD hardening over and above that from crystallographic effects and GND evolution, thus negating the need for a recovery term.

The density of geometrically necessary dislocations (GND), ρ_{GND}, is that which accommodates the lattice curvature and is determined from Nye's dislocation tensor $\boldsymbol{\Lambda}$ [25] given by

$$\boldsymbol{\Lambda} = \mathrm{curl}\left(\boldsymbol{F_p}\right) = \sum_{i=1}^{12} \rho_{Gs}^{i}\, \boldsymbol{b}^i \otimes \boldsymbol{s}^i + \rho_{Gen}^{i} \boldsymbol{b}^i \otimes \boldsymbol{n}^i + \rho_{Get}^{i} \boldsymbol{b}^i \otimes \boldsymbol{t}^i \tag{11}$$

where $\boldsymbol{s}^i, \boldsymbol{n}^i$ and $\boldsymbol{t}^i$ are the three orthogonal unit vector set, and ρ_{Gs}^{i} is the density of screw dislocations parallel to $\boldsymbol{s}^i$, ρ_{Gen}^{i} the density of edge dislocations parallel to $\boldsymbol{n}^i$ and ρ_{Get}^{i} the density of edge dislocation parallel to $\boldsymbol{t}^i$. Because there are 12 slip systems in FCC nickel crystals, the GND tensor comprises 36 independent variables (12 screw branches, 12 edge branches along $\boldsymbol{n}^i$, 12 edge branches along $\boldsymbol{t}^i$), which need to be solved from nine equations. These can be rewritten in matrix form

$$\widehat{\boldsymbol{\Lambda}} = \boldsymbol{A}\boldsymbol{\rho}_{\boldsymbol{GND}} \tag{12}$$

where $\widehat{\boldsymbol{\Lambda}}$ is a 9×1 column vector of Nye's dislocation tensor, and $\boldsymbol{A}$ a 9×36 matrix containing the basis tensors $\boldsymbol{b}^i \otimes \boldsymbol{s}^i$, $\boldsymbol{b}^i \otimes \boldsymbol{n}^i$, $\boldsymbol{b}^i \otimes \boldsymbol{t}^i$. $\boldsymbol{\rho}_{\boldsymbol{GND}}$ is a 36×1 column vector of GND components. However, the 36 independent GND components may give rise to a non-uniqueness problem through the above nine equations, hence an L_2 norm of GND density minimization is used to determine the local GND density [26] and an overall

density determined as

$$\rho_{GND} = \sqrt{\sum_{i=1}^{12}\left(\rho_{Gs}^{i}\right)^2 + \left(\rho_{Gen}^{i}\right)^2 + \left(\rho_{Get}^{i}\right)^2} \quad (13)$$

Elastic stored energy density is investigated as the primary driving force for fatigue crack nucleation, which has been reported for several alloys [6][27][28][29], and shows good agreement with experimental observation. The evolution of elastic stored energy density can be calculated from

$$G = \int \dot{G} dN \quad (14)$$

where $\dot{G}$ is the cyclic rate of elastic stored energy density, which can be obtained from

$$\dot{G} = \int \frac{\xi \boldsymbol{\sigma}:\mathrm{d}\boldsymbol{\epsilon}^{\boldsymbol{p}}}{\sqrt{\rho_{SSD}+\rho_{GND}}} \quad (15)$$

where ξ is the coefficient which specifies the fraction of dissipated energy which is stored in the material as dislocation structure. Here ξ is chosen to be 0.05.

2.2.1 Material properties

Tensile tests were carried out on $René\ 88DT$ samples with strain rates of 10^{-3} and $10^{-4}s^{-1}$. The corresponding macroscopic stress-strain curves are plotted in Fig. 3. The sub-FE model of the primary region of interest shown in Fig. 2, together with one additional representative microstructure, are utilized to calibrate the material properties which are given in Table 1.

Table 1 Material properties for $René\ 88DT$

C_{11}(GPa)	C_{12}(GPa)	C_{44}(GPa)	τ_{C0}(MPa)	b(μm)
273.6	170.7	125.8	420	$2.54\text{x}10^{-4}$

$\lambda(\mu m^{-2})$	$\nu(s^{-1})$	$\Delta F(J/atom)$	$\rho_{ssdm}(\mu m^{-2})$	$\Delta V(\mu m^3)$
12	$1.0x10^{11}$	$8.2x10^{-20}$	0.02	$22b^3$

The three independent stiffness constants were determined based on the experimental measurements recognizing the elastic anisotropic with a Zener ratio of 2.44 [30]. The activation energy ΔF may be estimated as $\Delta F = \omega G b^3$, where ω is a constant associated with dislocation obstacles, which depends on the energy barrier to dislocation motion [31]. It is chosen to be 0.04 for a non-strain rate sensitive response at room temperature. Correspondingly, the activation volume $\Delta V = \zeta b^3$ is determined to generate a small strain rate sensitivity at room temperature over the loading rates considered subsequently such that ζ is chosen to be 22.0. The initial density of mobile dislocations ρ_{ssdm} is estimated as 0.02 μm^{-2} [32]. Finally, ν is the dislocation jump attempt frequency, which can be estimated as 1×10^{11} [33].

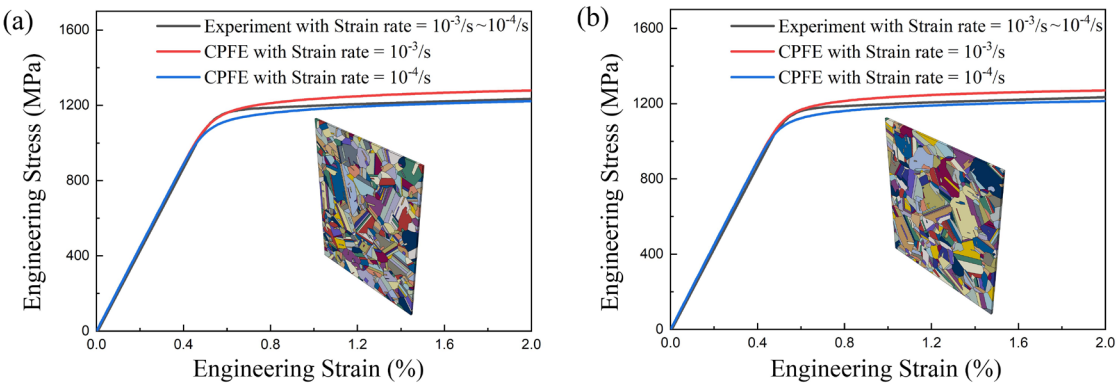

Figure 3. Engineering CPFE stress-strain responses and experiment results obtained for two differing regions of interest selected from the sample gauge region and explicitly

modelled [34]. (a) primary region of interest (as in Fig. 1). (b) A second region from the same gauge area.

The crystal plasticity sub-FE model (presented in Fig. 2 but inset in Fig. 3(a)) average stress versus strain response is shown in Fig. 3(a) for the two strain rates applied together with the experimental data. A second region of interest selected (arbitrarily) from the sample gauge area with different microstructure (and shown inset in Fig. 3(b)) was chosen and also modelled in order to perform a validation test; the CPFE results obtained against the experimental data are shown in Fig. 3(b) also showing good agreement. In addition, a comparison of strain and localization in the ROI including twin was carried out with the measurements averaged from the Heaviside DIC [13] and the CP calculated results, which are shown in Appendix 2. In the results section which follows, the CPFE models are utilized to investigate slip behaviour local to TBs which has also been captured from experiments using HR-DIC. These studies are then followed by presentation of the detailed assessments of local crystal elastic anisotropy and twin crystallographic orientation with respect to remote loading direction.

3. Results & Discussion

3.1 Strain, GND density, slip and stress state at TBs

CPFE results show that plastic strain localizes near TBs early in the stress-controlled cyclic loading (defined in Fig. 2(c)), which is shown within the ROI of the microstructure

(introduced in Fig. 2(b)), in Fig. 4(a). Further cycling leads to its continued evolution near TBs in the form of distinct bands directly associated with TB surface orientation and underlying slip system activations. Three typical strain localizations marked by white ellipses are shown in Fig. 4(a), and the bands in A form only on one side of respective TBs. However, those in B develop on both sides of the TBs. In C, local strain accumulation initiates from a triple junction and develops at TBs in the subsequent loading cycles (Fig. 4(b)). Most of the strain bands are found to be parallel to TBs (morphologically) except for one example in B. Here, parallel strain bands form initially (Fig. 4(a)), but subsequently, an inclined strain band develops to the TB in B, shown in Fig. 4(b). The heterogeneous strain field developed is clearly associated with microstructure involving both morphology and crystallography, as shown in Fig. 4(b). Finally, Fig. 4(c) shows the strain along path A-A' (in Fig. 4(b)) demonstrating the establishment of very clear strain peaks at the TBs which evolve cyclically.

Slip activation within the CP formulation is controlled solely by the slip system resolved shear stress (RSS) exceeding the current slip strength (see eqn. 6). The latter evolves with SSD and GND hardening (softening can also occur as plastic strain fields evolve to decrease strain gradients and hence GND density). As a consequence, it is found that the peak strains (see Fig. 4) are found often to be directly adjacent to TBs, and this results because of the anisotropic elastic mismatch generating local constraint and hence high RSSs, and the differing slip system orientations either side of the TB leading to preferred slip on one side only of the TB.

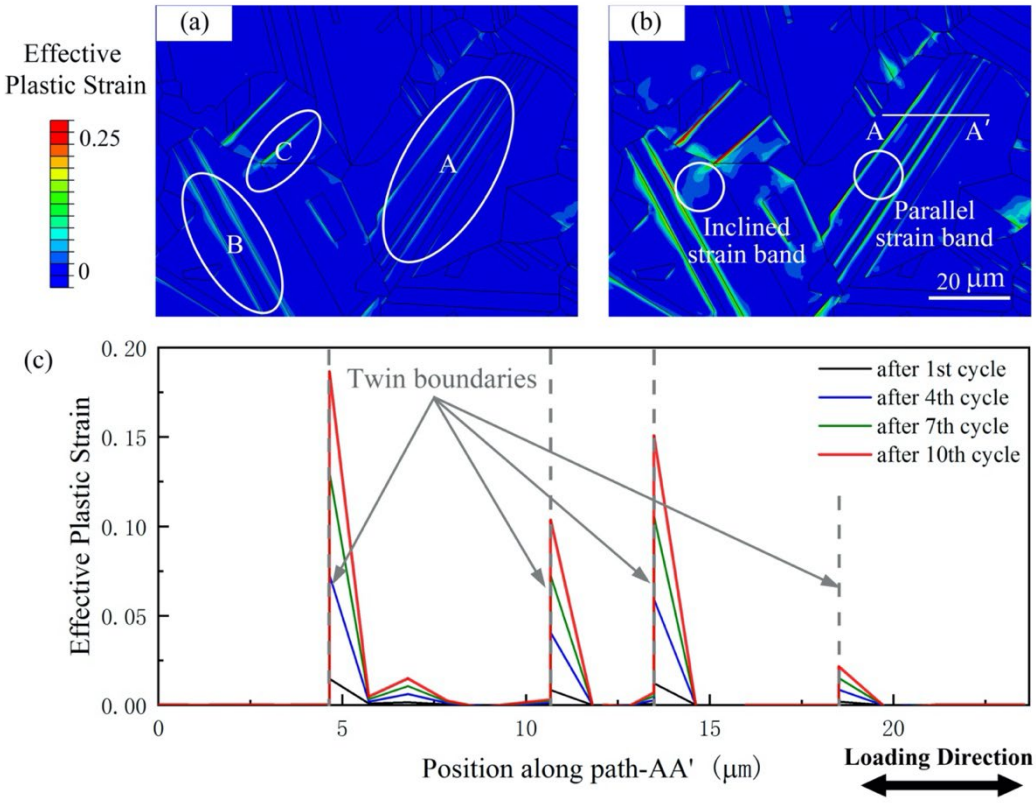

Figure 4. Effective plastic strain fields (a) ROI at 4th cycle, (b) ROI at 10th cycle, and (c) along path A-A' (shown in (b)) at cycles shown.

The corresponding CPFE-computed GND density distributions are shown in Fig. 5 and make clear that strong plastic strain gradients develop at TBs leading to high GND densities, reflecting lattice curvature, and in turn leading to the hardening of local slip strengths resulting from the higher sessile dislocation densities at these locations associated with TBs. Fig. 5(c) shows the GND densities along path A-A', and their cyclic evolution, in which both cyclic decreases and increases can be observed in the GND peaks, depending upon location. This occurs because the heterogeneous plastic strains initially established redistribute locally at the TBs during cycling, and this leads in some cases to

a more homogeneous strain field in turn resulting in reducing GND density with cycles as shown in Fig. 5(c). However, at other locations away from TBs, stronger strain gradients develop leading to increasing GND densities with cycles. Plasticity and the resulting establishment of residual stress can lead to a local non-zero mean stress state which drives local plastic ratcheting and hence the locally progressive cyclic hardening [13]. In addition, the peaks of GND density offset from the TBs in Fig. 5(c) result from the narrow strain bands which develop and align with TBs. These form from slip system activation parallel to the TBs, which is discussed later, and have also been observed in experiments and reported in [11].

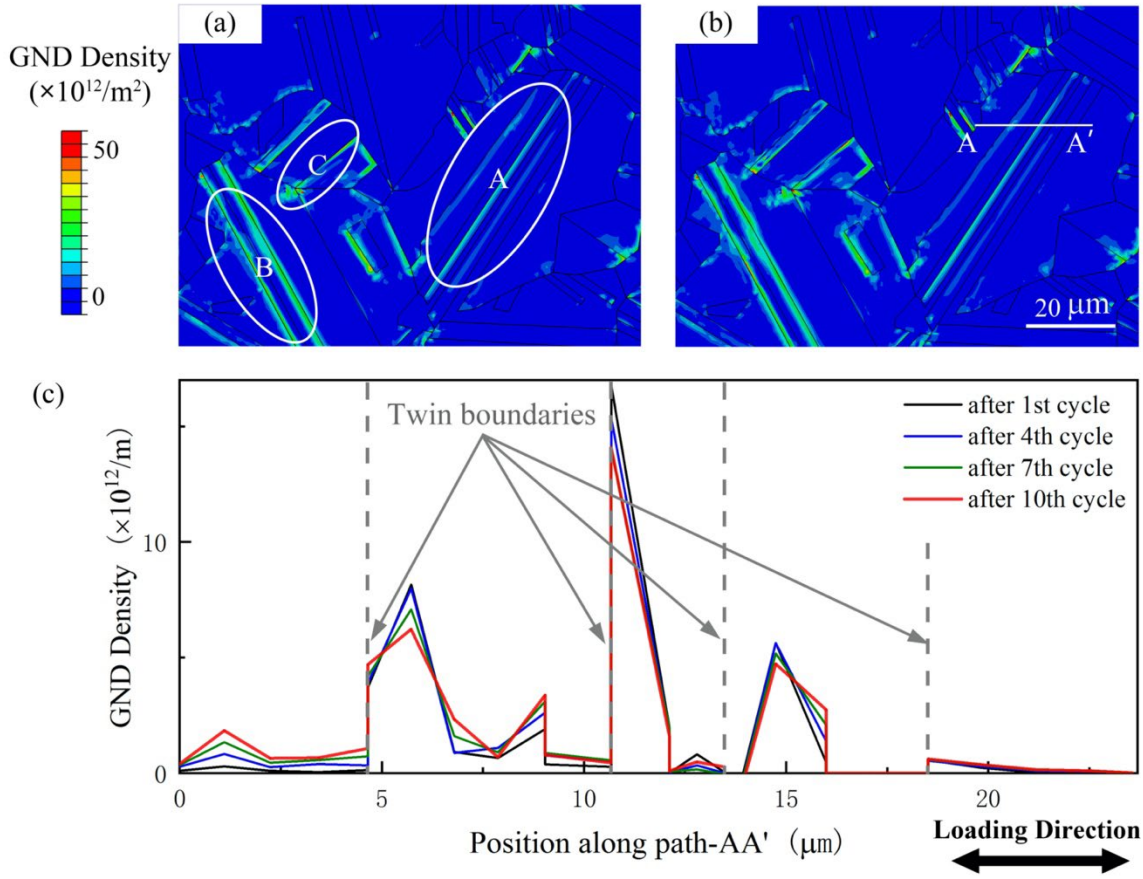

Figure 5. GND density fields (a) ROI at 4th cycle, (b) ROI at 10th cycle, and (c) along path

A-A' (shown in (b)) at cycles shown;

The CPFE-calculated crystal slip activations are investigated for particular grains of interest (GOIs) within the ROI (Fig. 2(a) and Fig. 4(a)), where slip system shear rate is given by eq. (6), and is activated once the resolved shear stress exceeds the slip system strength. The GOIs are shown within the ROI in Fig. 6(a), and in more detail for those within which single slip (Fig. 6(b)) and multislip (Fig. 6(c)) is activated respectively and which exhibit strong slip activations before cycle ten, all associated with the neighboring twins and the TBs. These groups of grains are highlighted in light red colour in Fig. 6. The activated slip systems can be classified as either parallel (PS) or inclined (IS) slip configurations with respect to the TBs [11], and these are detailed in Fig. 6 which shows the grain (and orientation) of interest, the relevant TB and its Miller indices, and the model predicted activated slip planes (in red) and directions (blue lines).

The Miller indices of the TB planes of interest, and the lattice cubes, are determined from knowledge of crystallographic orientations, obtained from EBSD scans before deformation. The anticipated free-surface slip traces are determined by obtaining the intersecting line between the red activated slip planes and the light blue surface rectangles.

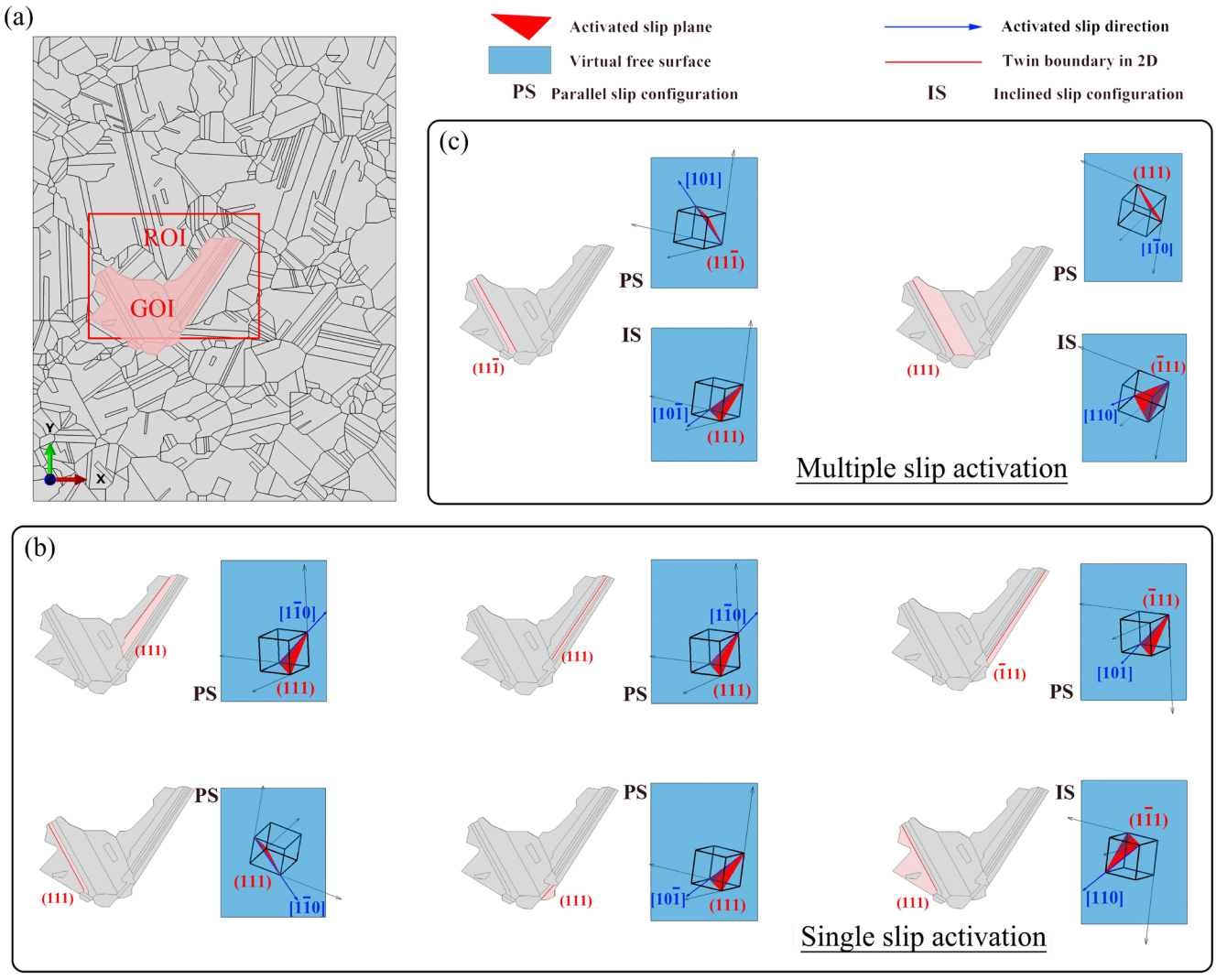

Figure 6. Slip activation in grains of interest within the ROI showing (a) the GOIs within the ROI, (b) grains giving rise to single slip activation, and (c) grains giving rise to multislip (both parallel [PS] and inclined [IS] to TBs) activation.

CPFE results show that single slip dominates within the GOIs in the early loading cycles, with six (of eight) grains exhibiting single slip activation (Fig. 6(b)), which include five which are parallel (PS) to the TB and only one with inclined (IS) orientation. These single slip activations are localized in the vicinity of the TB and lead to the plastic strain localizations observed in Fig. 4. The PS configurations comprise a series of slip planes that are parallel to the TB without impingement of the TB, resulting in the narrow plastic strain bands seen in Fig. 4(b). The high plastic strain gradient near the TBs can also be rationalized by the localized planar parallel slip. Compared with the PS configuration, the only IS configuration shows quite low slip accumulation; that is, there is no clear and discrete inclined plastic strain band observed in the ellipse B of Fig. 4(b) resulting from inclined slip. Hence, as reported in the independent experimental studies in [12][34][35], the CP model results also indicate that the PS configuration tends to dominate the slip localization. In addition to the single slip occurrences, multiple slip is observed in two grains (Fig. 6(c)), which develop two relatively uniform strain bands indicated by ellipse B in Fig. 4(a).

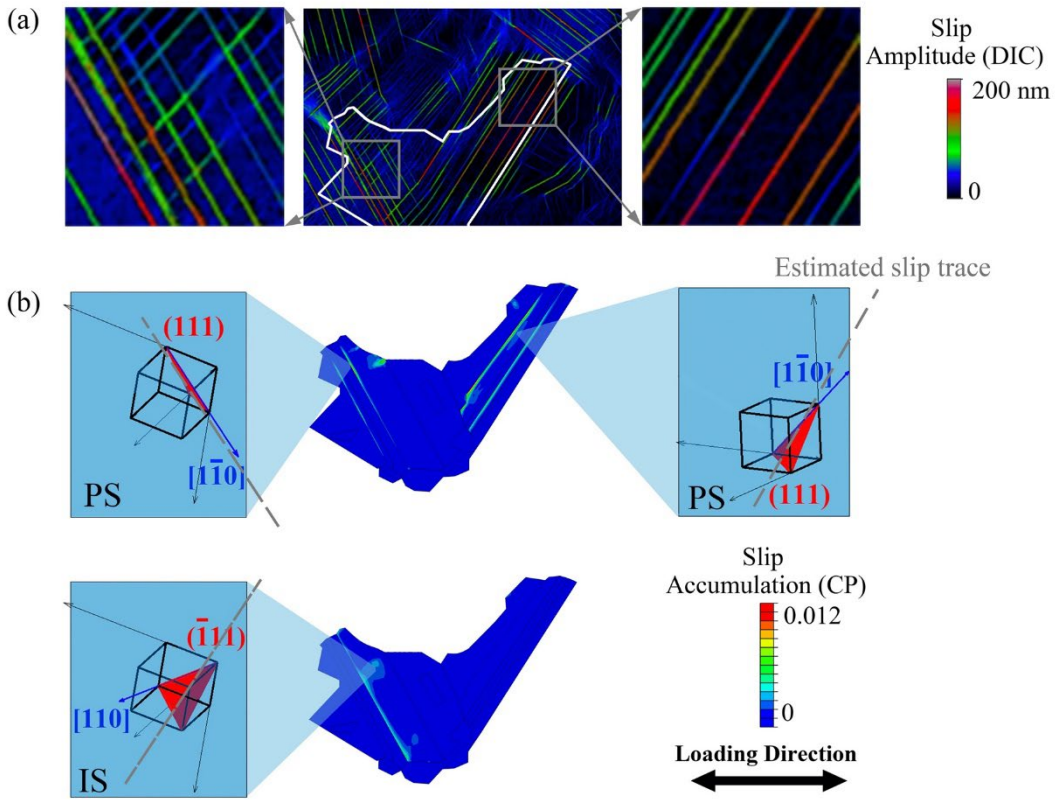

Figure 7. Slip localizations within GOIs after the 1st cycle (tensile part). (a) Slip amplitude measured from Heaviside DIC after the 1st cycle; (b) CPFE calculated slip activations after the 1st cycle.

The CPFE-calculated slip activations discussed above are compared with the Heaviside-DIC measurements reported in [13] to test the model prediction. The magnitude of slip accumulation on an individual slip system α is quantified in CPFE by

$$\gamma^{\alpha} = \int_0^t |\dot{\gamma}^{\alpha}| dt \tag{16}$$

In the HR-DIC measurement, the contributions from individual slip activations are

processed using a Heaviside function methodology giving rise to both slip amplitude and direction [13]. A qualitative comparison between the two methodologies is therefore possible. Fig. 7(a) shows the HR-DIC slip displacement amplitudes of the ROI with enlargements of the two sub-regions, demonstrating double slip and single slip. The corresponding CPFE results are shown in Fig. 7(b). The CP-computed slip traces (marked by grey dashed lines) firstly show good agreement with the experimental observations in these two selected local regions, and the single and double slip system activations shown at the two sub-regions in Fig. 7(a) respectively are also well captured.

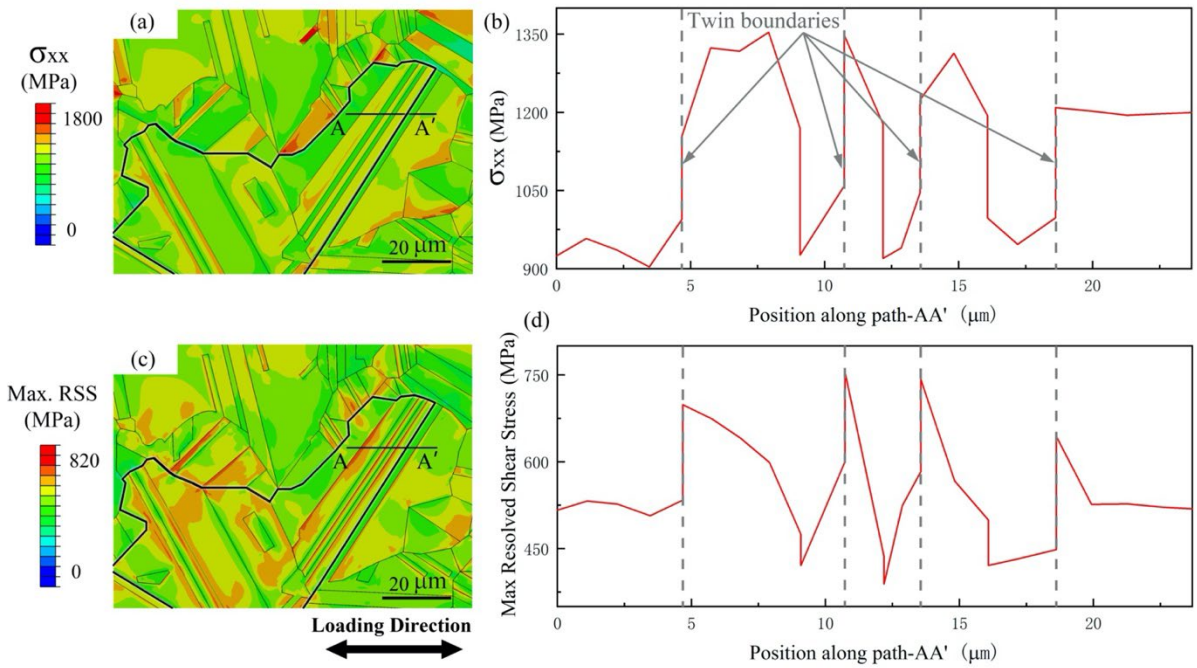

Figure 8. Stresses in the ROI extracted at the peak loading of the 10th cycle. (a) Loading direction stress field, (b) Loading direction stress along path A-A', (c) maximum slip system resolved shear stress field, and (d) resolved slip system resolved shear stress along path A-A'.

A potential key factor related to fatigue crack nucleation is the local stress field at the TB (since this, along with plastic strain and GND density) is important in determining the local stored energy density. The loading direction stress (σ_{xx}) and slip system resolved shear stresses within the ROI at the peak of loading cycle 10 are hence extracted.

Fig. 8(a) shows the σ_{xx} field corresponding to the ROI (Fig. 6(a)) where there is indication of strong concentrations at the two TBs. Fig. 8(b) reinforces this point showing the peak stress achieved at cycle 10 along the path A-A'. The local σ_{xx} (loading direction) component at the TBs are higher than the macroscale yield strength (1080MPa) such that plasticity is anticipated in these locations at the peak loading. The corresponding plots of maximum resolved shear stress (RSS) are given in Figs. 8(c) and (d), which show a stronger correlation with respect to the strain/slip localization at the TB, and Fig. 8(d) shows that the maximum RSS peaks align with the TB sites, and their magnitudes along path A-A' at the TBs are substantially higher than the critical resolved shear stress (420MPa), such that local slip activation, as observed in Fig. 7, is anticipated. The mechanistic explanation for the concentration of RSS at the TBs is that (i) strain compatibility at the TB with the constraint imposed from orientation and stiffness mismatch at the TB drives high elastic strains (influenced by the special crystallography of twins and the corresponding elastic stiffness anisotropy) and (ii) the high GND density arising because of the plastic strain gradients at the TBs (see Fig. 5) causing substantial initial (first cycle) slip system hardening of the respective SLIP STRENGTHs. Constraint effects develop at (e.g. twin) boundaries when the elasticity of the two grains is different,

and in this context, this arises easily because of the difference of the crystallographic orientations across the TB and the corresponding crystal elastic anisotropy. This also has been acknowledged in previous work [35][36]. Figs. 8(a) and (b) show σ_{xx} concentration near the TBs, reflecting to some extent the constraint effect caused by elastic stiffness difference, and this concentration is also apparent for the slip system RSSs (Figs. 8(c) and (d)). Hence the special crystallography of the twins is argued to be a primary reason leading to slip localization at TBs. The two key features, namely elastic difference (from stiffness anisotropy) and crystallographic orientation, with respect to loading direction, are quantitatively investigated in more detail in later sections.

3.2 Fatigue crack nucleation: observations and stored energy density

The slip and strain localization, together with stress concentration and GND density, have been quantified at TBs using CPFE, and where possible, compared directly with experimental observation. The stored (elastic) energy density has been argued to be a mechanistic driver of fatigue crack nucleation reflecting the establishment of dislocation structures and consequent configurational energy [8][36]. The latter is mostly stored as lattice curvature in GND structures [8][36] and the release of this energy per unit area is equated to new surface energy established with crack nucleation in fatigue. As a criterion to predict both the site of fatigue crack nucleation, and the cycles required to drive it, it has been demonstrated in single crystal, oligo crystal, and polycrystal nickel containing agglomerates [6][27][28]. Recent work [38] has demonstrated its non-singular nature at

crack tips, its relationship to classical fracture mechanics (K), and that it is a mechanistic driver of microstructurally-sensitive crack growth. It is utilized in this paper to investigate the experimental observations for crack nucleation at the TBs discussed above.

The stored energy density, defined in eqs. (14) and (15), is calculated for the microstructural ROI introduced above using the CPFE sub-model. Results are shown for the 10th fatigue cycle in Fig. 9, together with the experimental imaging to show the locations of observed fatigue cracking, notably but not exclusively, at TBs.

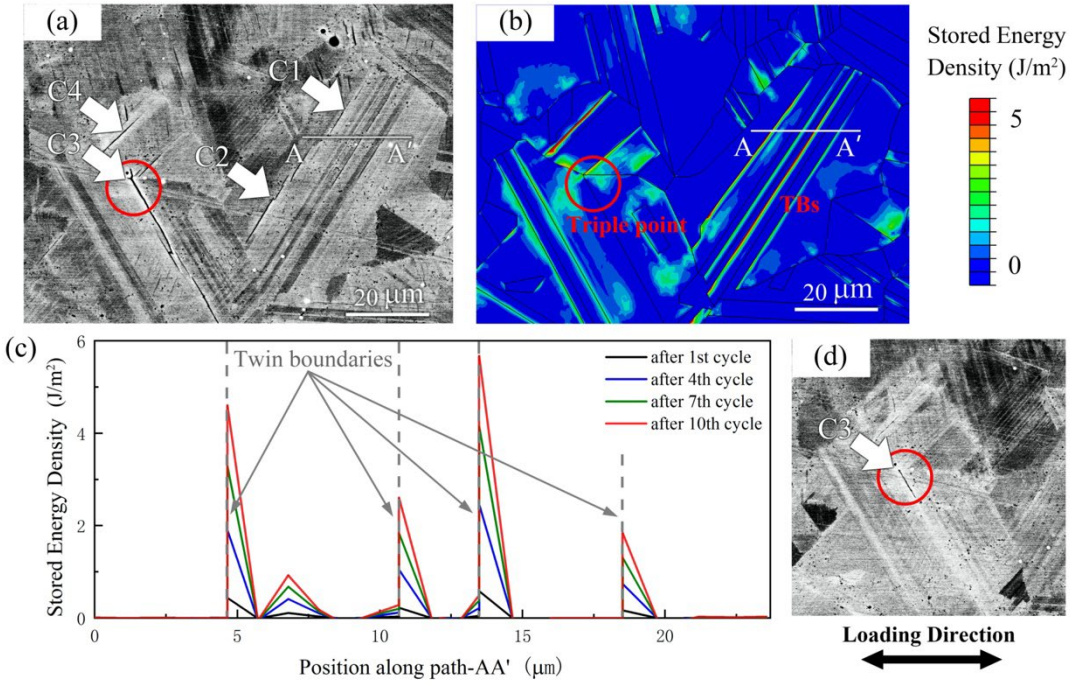

Figure 9. (a) SEM figure of ROI captured at the step end to failure; (b) Stored energy density field of ROI, calculated by CPFE after 10th cycle; (c) Stored energy density evolution along the path-AA'; (d) SEM figure of the early crack nucleation within the ROI.

The stored energy density path distribution in Fig. 9(c) may be compared with the corresponding distributions of strain (Fig. 4), GND density (Fig. 5) and stress (Fig. 8). As has been observed before [12], sites of high stored energy density are often, but not exclusively, associated with high strain, GND density and stress. However, it is now recognized that local plastic strain, generated by slip, is a necessary but not sufficient requirement for fatigue crack nucleation. The role of GND density and stress is to moderate the stored energy density and as a consequence, the locations of the highest peaks of stored energy do not necessarily correlate directly with peaks of GND density (Fig. 5) or stress (Fig. 8). Whereas the stored energy density has been shown to match unambiguously experimental observations of fatigue crack nucleation site, slip, GND density and stress have not [6]. The particular aspects of stored energy, including its microstructural sensitivity, its relationship to classical stress intensity, K, and its non-singular nature at crack tips are discussed in [38].

A number of fatigue cracks can be observed in Fig. 9(a), and most of them are associated with the TBs, and the stored energy density captures all observed cracks within the ROI. For the cracks which develop parallel to TBs (cracks C1 and C2 in Fig. 9(a)), they nucleate and grow at the twin lamellar as shown in Fig. 9(a). This is reflected in the stored energy density shown in the contour plot in (b) and in more detail along the path A-A' in (c). An additional fatigue crack type (C3) is observed to nucleate from a triple junction and subsequently grow along the associated TB as shown by the red circles in Fig. 9(a), (b); the early nucleation of this crack is shown in Fig. 9(d) confirming its origin

as the triple junction, as predicted by stored energy.

Outside of the ROI shown in Fig. 9, other crack nucleation sites are observed in the experiment. The primary focus of this study is the understanding of mechanistic drivers of preferential fatigue crack nucleation at annealing twins, and TBs, in the nickel alloy considered. Hence we confine our study to the ROI. However, we note the simplifications made in the modelling in which edge effects may be introduced by selection of model boundary conditions that do not perfectly align with those which apply in the experimental microstructures. In addition, the simplification of considering only free surface grain and twin morphology and crystallography is known to have adverse consequences for identifying all fatigue crack locations in the modelling. However, the microstructural ROI contains persuasive experimental evidence for fatigue crack nucleation at TBs, and a further crack in the same ROI nucleating at a triple junction; the TB cracks develop unequivocally on a particular side of the twin lamellae. All of these features are correctly captured by the stored energy density. It is argued, therefore, that this is sufficiently persuasive to warrant more detailed model investigations of the roles of both local twin elastic anisotropy and crystallographic orientation in fatigue crack nucleation at TBs, since both have been hypothesized as mechanistic drivers of preferential crack nucleation [10][12][13][35].

3.3 Elastic anisotropy in TB crack nucleation

Nickel has intrinsically high anisotropic elasticity, such that the Young's modulus parallel to <111> is higher than that for <100>, leading to strong anisotropic mechanical behavior in single crystals. Several experimental and modelling studies have demonstrated that quantitative fatigue failure criteria cannot be rigorously established without consideration of elastic anisotropy [35][39][40]. In this section, a systematic study based on the CPFE ROI model is performed to understand the role of elastic anisotropy in driving fatigue crack nucleation with an emphasis on annealing TBs.

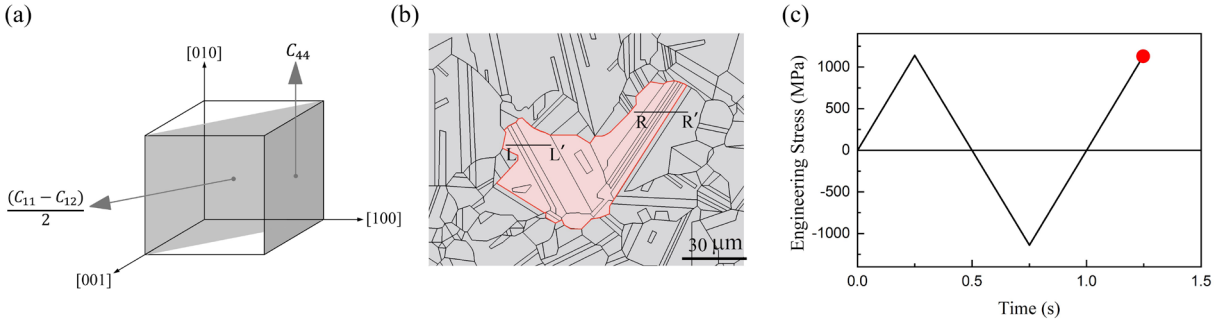

Figure 10. (a) Physical meaning of the three independent stiffness constants; (b) The grains of interest for which elastic anisotropy is studied; (c) The point of peak loading considered.

At the continuum level, the elastic properties of an FCC material can be fully determined by three independent stiffness constants C_{11}, C_{12} and C_{44}. The Zener ratio, given in eq. (17), is employed to quantitatively characterize the magnitude of the elastic anisotropy in this study. The physical meaning of Zener ratio may be considered by reference to Fig. 10(a) where C_{44} is the modulus of {100} planes elastically shearing

along <010>, and $(C_{11} - C_{12})/2$ the modulus of {110} planes elastically shearing along <$\bar{1}$10> [41]. If $C_{44} = (C_{11} - C_{12})/2$, that is Zener ratio = 1, then the elastic stiffness becomes isotropic.

$$\text{Zener ratio} = \frac{2C_{44}}{C_{11} - C_{12}} \tag{17}$$

Sangid et al. [42] have reported that the normal stress with respect to the TB plane is important in plastic strain development (and hence potentially for crack nucleation). Despite the heterogeneous stress field at the TB, the normal stress may play a significant role because E<111> is higher than for other crystal directions (eg. E<100>), and this elastic difference is coupled with the Zener ratio. Hence, this stress state may encourage mixed-mode failure at the TB, consisting of a slip-driven shearing nucleation in mode II and mode I crack opening resulting from the high normal stress. Considering the interesting reports of the effect of (111) normal stress in stress concentration [42], and the twin relationship to its parent grain through the orientation relationship, Two approaches are chosen to investigate the effect of elastic anisotropy by considering particularly $E_{<111>}$ and $E_{<100>}$ in turn, for the parent grain/twin region shown highlighted in red in Fig. 10(b). In the first approach, $E_{<100>}$ is fixed and $E_{<111>}$ varied to give a range of Zener ratios (including that corresponding to elastic isotropy). In the second, $E_{<111>}$ is fixed and $E_{<100>}$ varied. Note that both approaches correspond to changing the Zener ratio, with higher ratio indicating stronger elastic anisotropy. However, each approach corresponds to a different form of anisotropy. In each approach, four differing Zener ratios from 1 to 2.44 are generated, and full elastic parameters are shown by a 3D surface graph of respective

Young's moduli in Fig. 11(a) and Fig.12(a). The anisotropic conditions which apply to the crystal modelling above are indicated as 'actual'. The surfaces are plotted to show Young's modulus as a function of orientation, where the Young's modulus for a specified direction is given by

$$\frac{1}{E_{<hkl>}} = C_{11} - 2\left[(C_{11} - C_{12}) - \frac{1}{2}C_{44}\right]\left(l_x^2 l_y^2 + l_y^2 l_z^2 + l_x^2 l_z^2\right) \quad (18)$$

where l_x, l_y and l_z are the direction cosines for crystal directions <hkl> with respect to global xyz axis. Fig 10(b) shows highlighted (in red) the two twinned regions within the ROI considered in the analysis and the two paths (R-R' and L-L') examined. The path R-R' considers the single parallel slip configuration (PS) that is observed in the right twinned region. Path L-L' presents the multislip configuration (PS+IS) observed in the left twinned region. The elastic properties of the respective twin-parent regions (red region in Fig. 10(b)) are varied, maintaining the twin – parent grain crystallographic orientations, whilst keeping all other grain elastic properties unchanged (grey region in Fig. 10(b)). The loading shown in Fig. 10(c) is imposed to carry out independent CPFE simulations with each set of elastic constants (including those which accurately reflect the 'actual' elastic anisotropy in the earlier sections of the paper) for both the right-hand and left-hand twin-parent sets. The results of these studies are shown in Fig. 11 and Fig. 12 respectively, which are extracted at the peak loading point shown in Fig. 10(c).

The maximum resolved shear stresses corresponding to the two different elastically anisotropic approaches are shown in Figs. 11(b) and 12(b) respectively for path R-R'. Fig. 11(b) and 12(b) show that higher maximum RSSs are developed at the TBs with

increasing $E_{<111>}$ and decreasing $E_{<100>}$ respectively, both corresponding to higher Zener ratio. However, increasing $E_{<111>}$ is found to give much higher TB RSSs than an equivalent level of elastic anisotropy from decreasing $E_{<100>}$. Comparing the two isotropic cases (Zener ratio=1) shows that much more uniform RSS fields along path R-R' are developed, suggesting similarly more homogeneous, and less localized, slip activation. In addition, the higher (isotropic) modulus which results from the set of isotropic elastic constants selected in the second approach (Fig. 12) naturally gives rise to higher average stresses, even if the concentrations at TBs are reduced compared to the first approach (Fig. 11).

The corresponding GND densities along path R-R' are shown in Fig. 11(c) and Fig. 12(c). In both cases, GND densities are developed at TBs and increase with elastic anisotropy (Zener ratio). As in the earlier analysis, this results from the heterogeneous plastic strain field developed by the discrete parallel slip aligned with the TBs. Higher elastic anisotropy (Zener ratio) drives this heterogeneity to a sharp gradient around the TBs, reflected by the peaks in Fig. 11(c) and Fig. 12(c), in which some of the peaks are seen to be shift away from the TBs (grey lines).

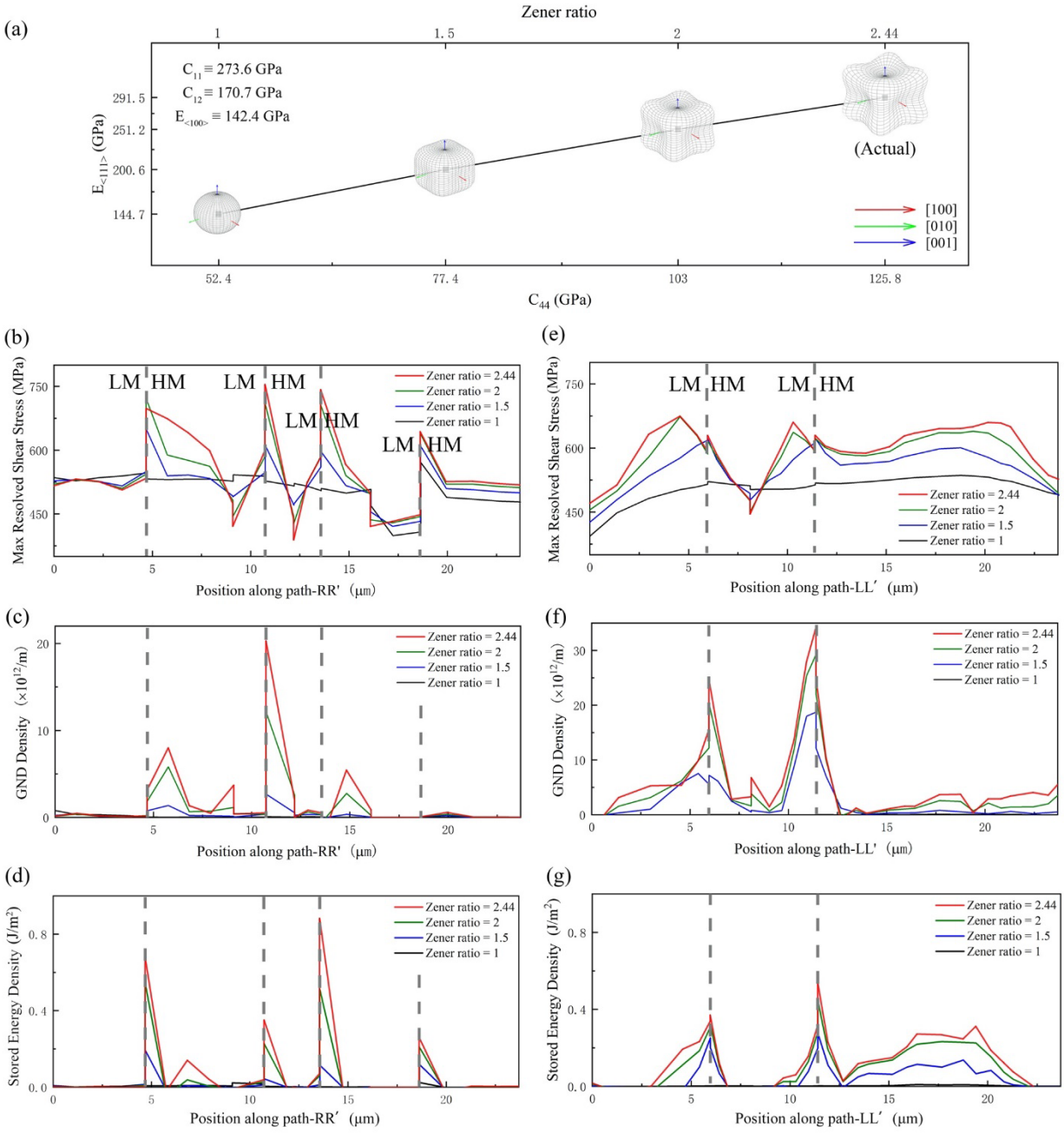

1 Figure 11. Varying elastic anisotropy Zener ratio with fixed E<100> showing (a) elastic
2 properties for four differing Zener ratios; (b) maximum RSS along path R-R'; (c) GND
3 density along path R-R'; (d) stored energy density along path R-R'; (e) maximum RSS
4 along path L-L'; (f) GND density along path L-L'; (g) stored energy density along path
5 L-L'. Dashed lines indicate locations of TB. HM and LM indicate high and low uniaxial

moduli respectively with respect to each TB.

The corresponding stored energy densities along path R-R' are shown in Figs. 11(d) and 12(d). In both cases, the stored energy density peaks at the TBs for high Zener ratios (ie higher elastic anisotropy). Interestingly, for the first anisotropic approach, the peaks in stored energy are unambiguously only associated with TBs. While the peaks at TBs are retained for the second form of anisotropy, the stored energy is more uniformly distributed, even removed from the TBs. For the case of isotropic elasticity, the stored energy density effectively vanishes at the TBs for the first anisotropic approach but does not do so for the second approach but remains more uniform and uninfluenced by the TBs.

Finally, we consider the resolved shear stresses and the stored energy densities which result from the two elastic anisotropy approaches but now for the different location in the microstructure corresponding to path L-L' in Fig. 10(b). Recall that in this region, multiple slip system activation occurs, including slip inclined (IS) to the TBs as well as parallel (PS) to them in the twinned region. Figs. 11(e) and 12(e) show much more uniform distributions of resolved shear stress for both anisotropic approaches, though both show that increasing elastic anisotropy (increasing Zener ratio) leads to more localisation at the TBs. The stronger uniformity reflects more slip activations and hence more uniform slip and strain fields. Interestingly, contrary to the parallel slip behaviour at R-R', the peaks of the GND density along L-L' are located at the TBs without offset as shown in Fig. 11(f) and Fig. 12(f). This results because of the parallel and inclined slip interaction with the

TBs. Local peaks in stored energy density, shown in Figs. 11(g) and 12(g), develop in both elastic anisotropies, very much strengthened by increasing Zener ratio. However, Fig 12(g) shows that even for highest levels of anisotropy (Zener ratio of 2.44), there exist potential states of elastic anisotropy for which stored energy density is higher at locations away from TBs. However, the combination of elastic stiffnesses giving rise to this are, of course, artificial (for the purposes of this systematic study) and do not reflect the true anisotropic properties which are representative of $René\ 88DT$.

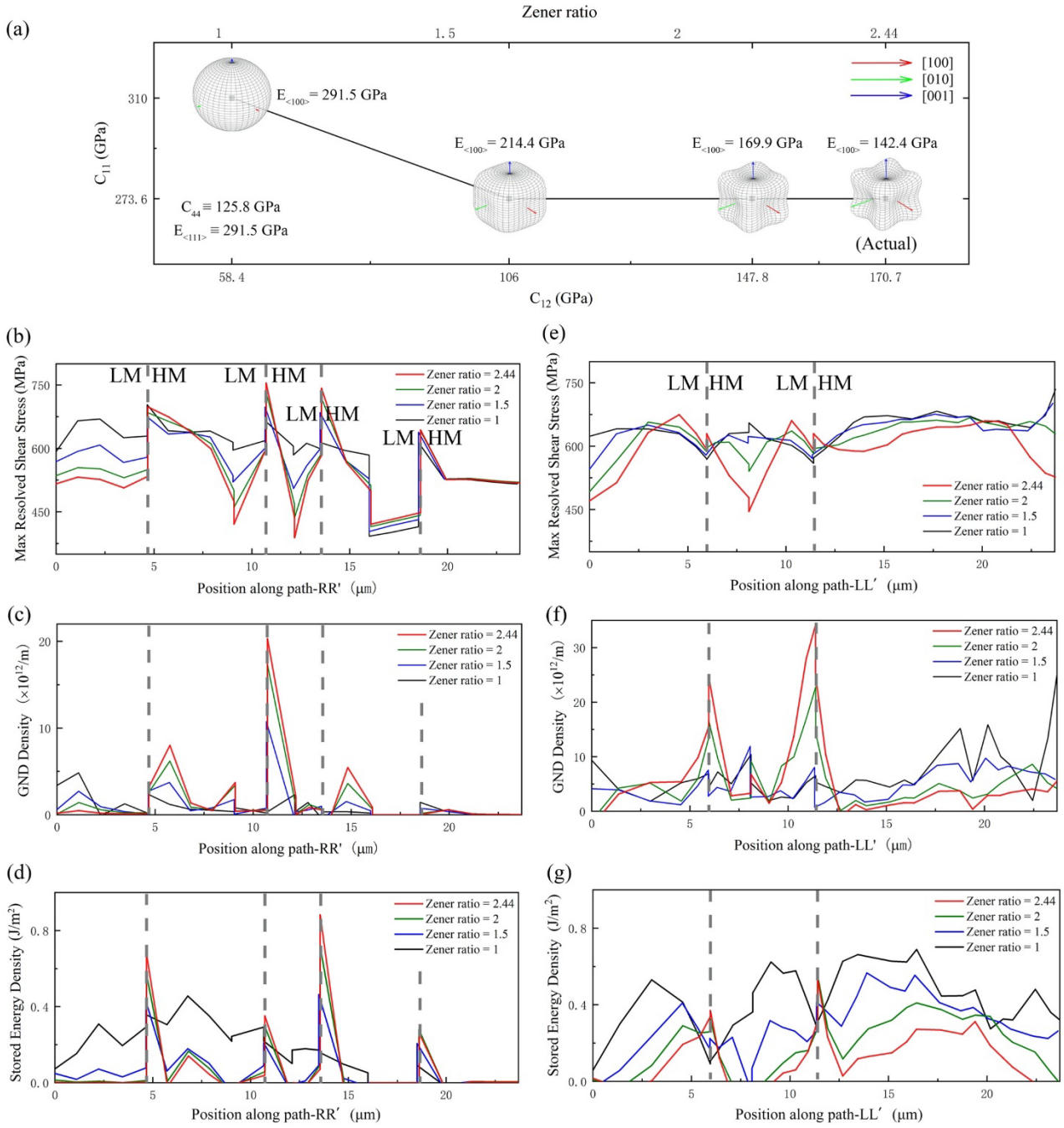

1 Figure 12. Varying elastic anisotropy Zener ratio with fixed E<100> showing (a) elastic
2 properties for four differing Zener ratios; (b) maximum RSS along path R-R'; (c) GND
3 density along path R-R'; (d) stored energy density along path R-R'; (e) maximum RSS
4 along path L-L'; (f) GND density along path L-L'; (g) stored energy density along path
5 L-L'. Dashed lines indicate locations of locations of TBs

3.4 Twin crystallographic orientation sensitivity

Nickel single crystal behaviour is both elastically and plastically anisotropic such that crystallographic orientation with respect to remote loading is important to the resulting material response. This holds also for annealing twins and their parent grains within a loaded polycrystal. An important constraint is that of the orientation relationship which holds between parent grain and twin. In nickel with FCC structure, this important constraint can be expressed as a 60° twist angle along their common <111> crystal direction. In addition, previous studies have demonstrated that fatigue cracks preferentially nucleate at TBs when the TB trace holds a 45° angle with respect to remote loading direction [16][35]. This "morphological worst case" is known so that it becomes useful to investigate the overall crystal orientation of the parent grain-twin couple with respect to remote loading in order to establish if a worst case crystallographic orientation exists which mechanistically favours fatigue crack nucleation. If this were to be the case, it would be anticipated that a higher proportion of crack nucleations at TBs in polycrystals would be found to be associated with a given (parent grain) crystal orientation when the surface TB traces are inclined at 45° to the remote loading direction. Hence a systematic study has been carried out utilizing the same microstructural CPFE model ROI presented above, properly capturing the parent-twin orientation relationship, and examining stored energy density (and other important quantities) developing at TBs as a consequence of parent grain orientation with respect to loading.

The microstructural ROI 2 shown in Fig 13(a) is considered, for which the TB traces are at or near 45° to the remote loading direction, corresponding to the morphological worst case. In ROI 2, the parent grain and twin, designated Grain A and Grain B respectively, are assigned systematically a range of orientations with respect to loading direction, and each case is analyzed with the CPFE model. All other grain orientations and morphologies within the polycrystal model remain unchanged. The crystal orientations considered are those which result from the grain-twin crystal orientations rotated about their common <111> direction (maintaining the parent-twin crystal orientation relationship) in steps of 10° without change to the parent-twin morphology. Hence this is a purely crystallographic study. Twelve differing crystal orientations are generated, such that all of the crystal configurations considered have their (111) planes parallel to the TB and the rotation axis [111] is parallel to the normal to the TB plane. CPFE modelling is performed using these twelve crystal orientations independently subject to the same loading introduced in the previous section. Due to the high symmetry in FCC, there is a 120° periodicity about <111> so that orientations are varied from -60° to +60°. The computational results are extracted at the peak loading point following the first cycle as shown in Fig.10(c).

Fig.13 shows the four investigated quantities (effective plastic strain, maximum RSS, GND density, and stored energy density) and how they vary as the crystal orientation is changed about the [111] direction. The -60° and +60° orientations show identical results,

confirming the 120° periodicity about the <111> crystal direction in FCCs. The peak values of all these quantities can be observed to occur for the parent-twin configuration with an orientation of about -20° with respect to the original, unrotated crystal orientation (i.e. that obtained from the experimental characterization, and designated as the 0^o orientation in the figures). All the quantities observed are localized on the elastically less stiff side of the TB in a range of orientations from -10° to -30° except for the actual case of 0^o, and those which depend on slip activation effectively vanish when the orientation angle diverges outside of this range (eg +20° orientation in Fig. 13) for which the orientation is unfavourable for slip. However, high plastic strains and corresponding stress concentration (resulting from hardening) can be developed for particular crystal orientations; these conditions lead to local high stored energy densities which, as demonstrated earlier, progressively increase with cyclic loading, favouring fatigue crack nucleation at the TB for very particular parent-twin crystallographic orientations.

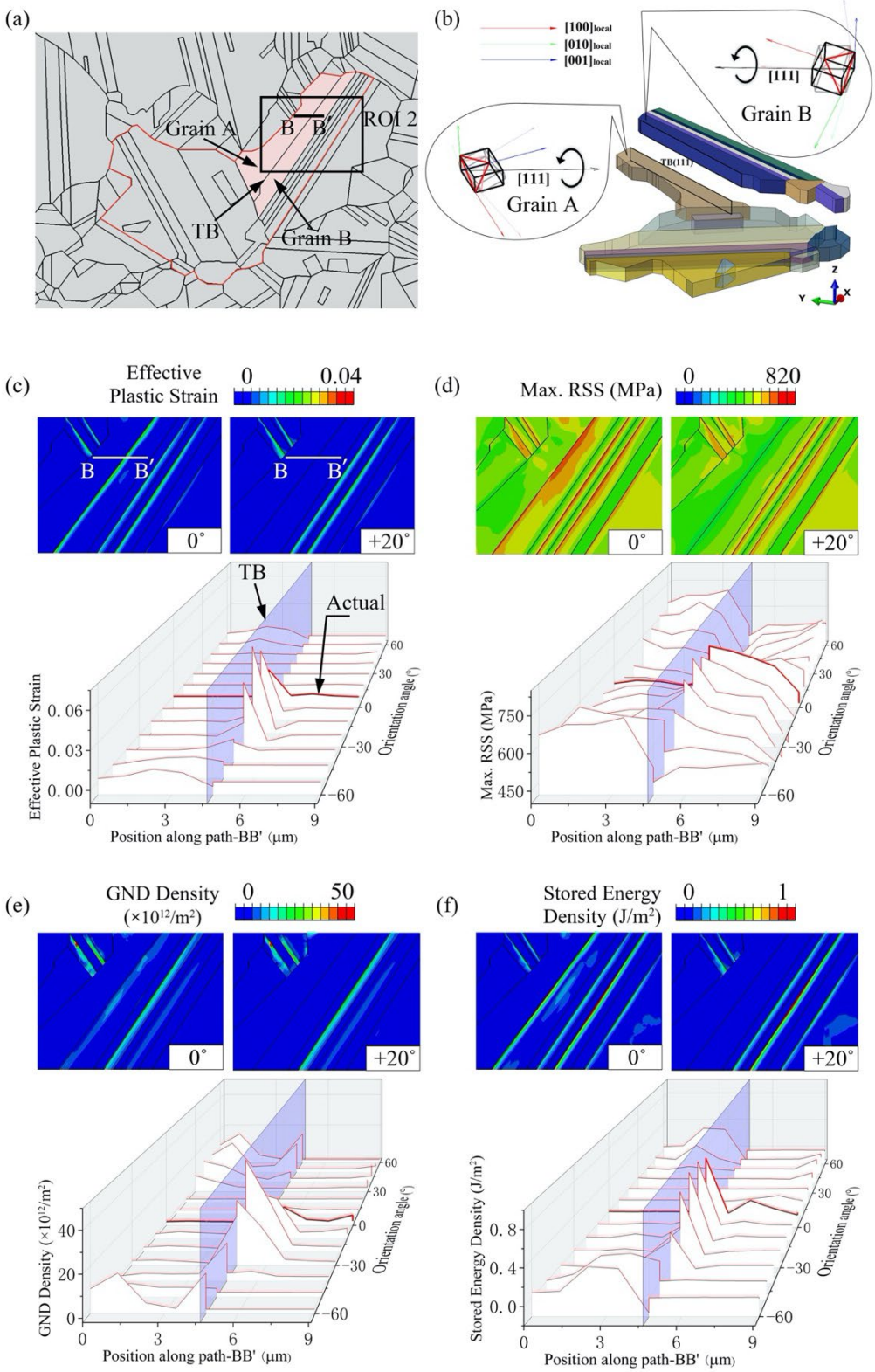

Figure 13. Sensitivity study of TB quantities to crystallographic orientation showing (a) The grains highlighted by red are studied for crystallographic orientation; (b) Schematic

diagram showing crystallographic rotation; (c) Effective plastic strain; (d) Maximum resolved shear stress; (e) GND density; (f) Stored energy density; the 3D path plots correspond to B-B' in Fig. 13(a). The 'actual' crystal orientation has been marked by bold red lines. The location of TB is shown as a violet plane.

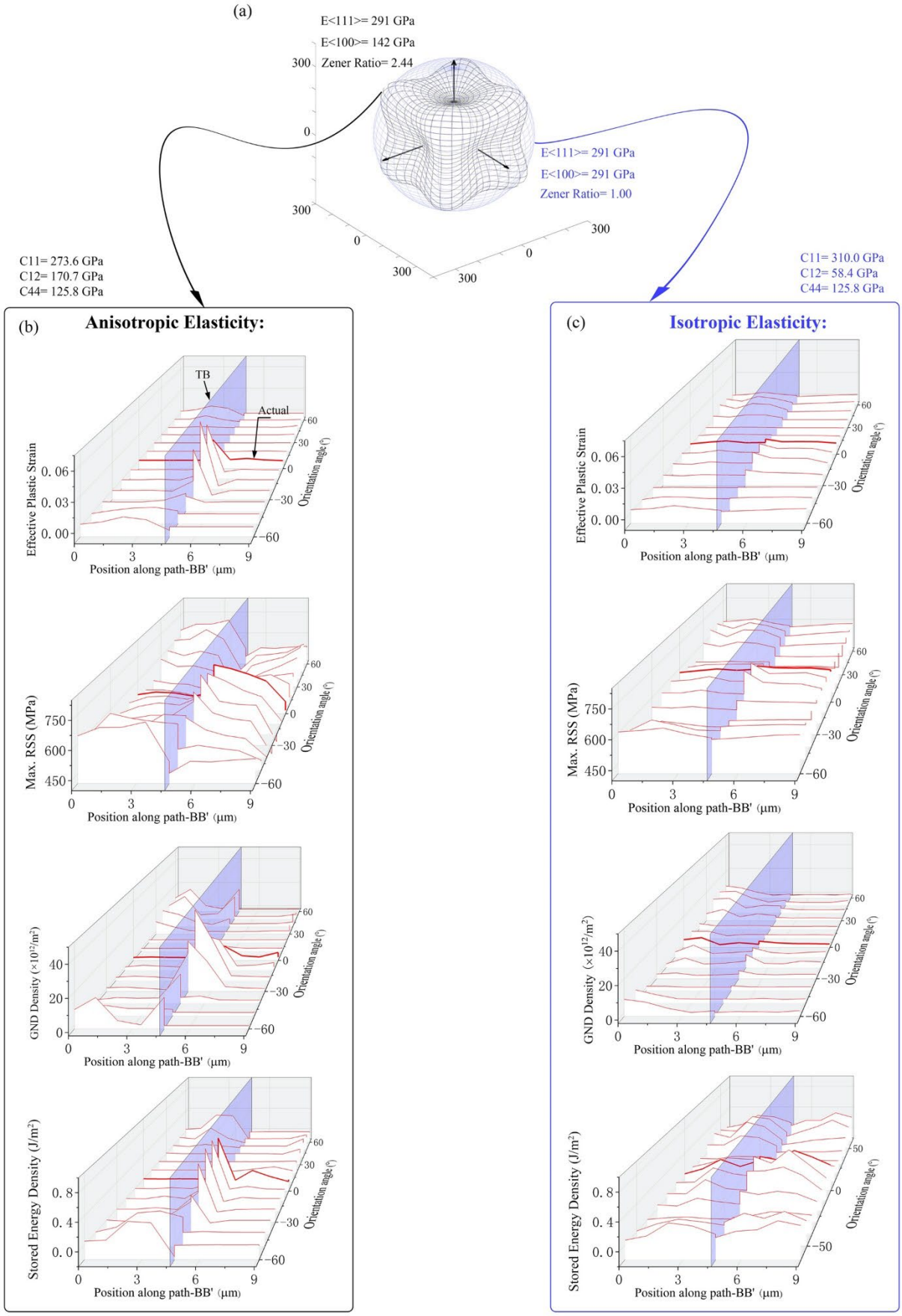

1 Figure 14. Sensitivity study of TB quantities to crystallographic orientation showing

results for the particular cases of anisotropic and isotropic elastic twin-parent grain properties shown in (a), where (b) shows results for anisotropic elasticity and (c) results for isotropic elasticity. The 3D path plots correspond to B-B' in Fig. 13(a). The 'actual' crystal orientation has been marked by bold red lines. The location of the TB is shown as a violet plane.

Fig. 13 shows sensitivity of fatigue crack nucleation to TB crystallographic orientation, in terms of high local stored energy. Fig. 11 and Fig. 12 quantitively demonstrate the importance of elastic anisotropy in fatigue crack nucleation but only for the original, unrotated crystal orientation case. Here, we compare the sensitivity of key results to crystallographic orientation for the cases of elastic anisotropy and isotropy across the TB along path BB' (shown in Fig 13(a)), for the worst-case TB morphological orientation of about 45°. The isotropic elastic properties considered, together with the original anisotropic elastic properties, are shown in Fig. 14(a) in blue and black respectively. These two elastic cases have identical <111> Young's and shear moduli, but their <100> moduli are different. The loading conditions applied are identical to those used in generating Fig. 13. Fig. 14 shows the resulting plastic strain, maximum resolved shear stress, GND density and stored energy density for the two cases. Fig. 14(c) demonstrates that elastic isotropy leads to much more uniform (and low magnitude) quantities across the TB compared with the case of elastic anisotropy, and that contrary to the case of anisotropic elasticity, no clear peaks can be observed for the twelve crystal

orientations considered. Hence, the elastic anisotropy drives not only the preferential localization of plasticity and fatigue crack nucleation at the TB, but also facilitates the sensitivity to crystal orientation. Fig. 14 reinforces the importance of anisotropic elasticity in fatigue crack nucleation at annealing twins in polycrystal nickel-based superalloy.

Finally in this section, an analysis of the effect of parent grain-twin orientation on slip system activation, in terms of the elastic anisotropy and crystal orientation is provided in the context of independent experimental observations of crack nucleation compared with CPFE model predictions from the current work. Young's modulus along the loading direction (E_{LD}) has been reported as a significant factor in fatigue crack nucleation at TBs. Larger differences between parent grain and twin E_{LD} have been reported to encourage the triggering of fatigue crack nucleation [12]. Here, a parent grain - twin pair (Grain A and Grain B in Fig. 13(a)) which has been observed to nucleate a fatigue crack (see C1 in Fig. 9(a)) is chosen to investigate the effect of crystal orientation in slip localization and fatigue crack nucleation. The calculated loading direction moduli E_{LD} of both parent and twin as a function of orientation with respect to loading are shown in Fig. 15(a), and the corresponding slip system (global) Schmid factors for the twelve independent slip systems for both parent and twin are shown in Fig. 15(b) with orientation. Of all the crystal orientation configurations considered, four configurations with strong slip localization and fatigue crack probability are marked by violet circles in both Fig. 15 (a) and (b). The particular case of the experimental sample detailed in section 3.2 above for which fatigue crack nucleation is observed to occur in experiment is highlighted by a

cross, both in the modulus and Schmid factor plots. The stored energy density in the local region of Grains A and B is shown in Fig. 15(c) with the corresponding SEM crack observation.

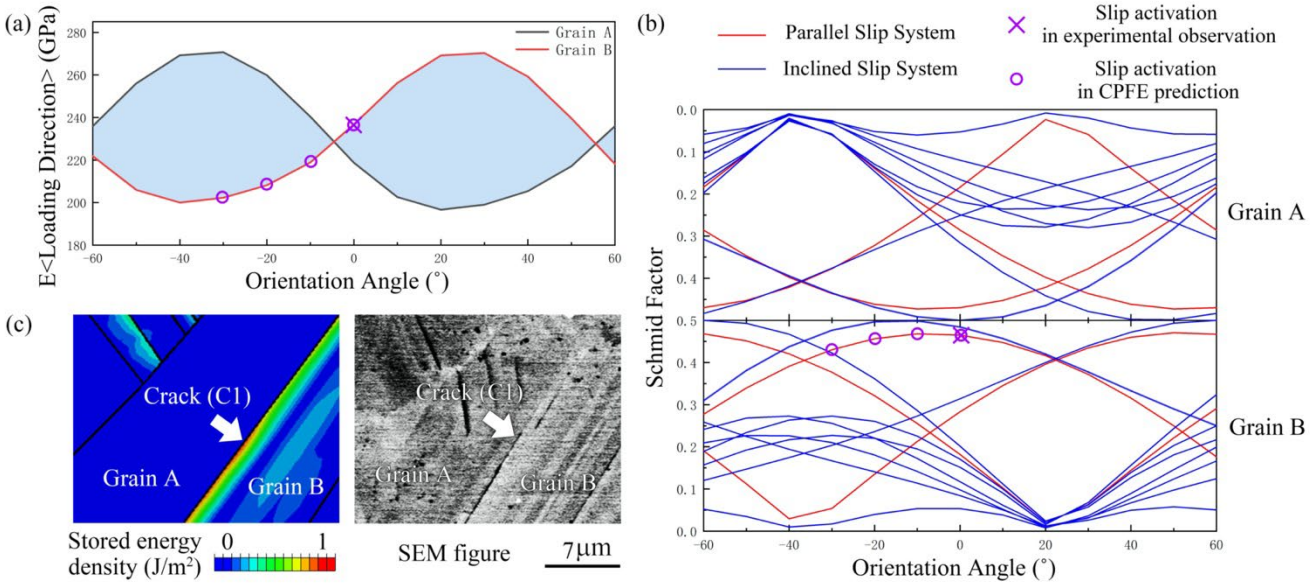

Figure 15. (a) Variation of Young's moduli (loading direction) of parent grain and twin with crystal orientation. (b) Schmid factors of twelve slip systems with orientation; (c) Stored energy density at the TB after 10^{th} cycle for orientation of 0^{o} (ie the experimental sample reported in this paper).

The E_{LD} difference between the parent grain and twin is apparent from the respective moduli shown in Fig. 15(a). Fatigue crack nucleation is identified as marked in Fig 15(c) and Grain B has a slightly higher E_{LD} than that of Grain A for the reference orientation (ie 0^{o} orientation corresponding to the experimental observations presented, marked by a cross-circle in Fig. 15(a) and (b)). The CPFE predicts crack nucleation in the range of

orientations from -10° to -30° (marked by the circles in Fig. 15(a) and (b)). Unlike the sample orientation, these three parent/twin pair orientations show that the crack site is located within Grain B, which has lower E_{LD} than that of Grain A. This is in agreement with previous independent experimental observations [12] (though it is described as being the elastically 'softer' side). Note that both this paper and [12] consider the elastic stiffness (or 'softness'), E_{LD}, to be determined by assuming a uniaxial stress state resulting from the remote loading direction. Fig. 15(a) shows this assumption is reasonable but is not completely accurate due to the heterogeneous stress field.

With respect to slip system activation, parallel slip is predicted to be activated in all of the four locations where cracks are observed to nucleate. However, an interesting point is the global Schmid factors of these activated slip system are high but not the highest. Hence global Schmid factors can identify slip activation but due to local elastic constraint effects, are not always accurate. No inclined slip systems are activated in any of the alternative crystal orientations, which means the parallel slip configuration must dominate and crack nucleation in these cases.

4. Conclusions

Integrated experiments, characterization and CP modelling of annealing twins in *René* 88*DT* under cyclic loading have been studied in order to obtain mechanistic understanding of fatigue crack nucleation and why this is driven to occur preferentially at TBs. Specifically, the effects of elastic anisotropy and parent grain / twin crystallographic orientation with respect to loading have been investigated for a given fixed microstructure. The key conclusions are:

1. Strong slip localization, and correspond plastic strain gradients, occur at TBs driven by elevated resolved shear stresses during cyclic loading. Slip parallel to TBs was found to dominate and good agreement was obtained between SEM Heaviside-DIC strain measurement and CPFE modelling at TBs. As a consequence, TBs were found to lead to strongly elevated local stored energy densities reflecting experimental observations of preferential TB fatigue crack nucleation.

2. Elastic anisotropy was found to be key to developing elastic constraint at TBs, in turn affecting resolved shear stresses and hence slip system activation, which was not always correctly identified by global Schmid factors. Systematic variations of the Zener anisotropy factor demonstrated that increasing elastic anisotropy drove higher resolved shear stresses, more highly localized slip activation, and consequent GND density and stored energy density, thus explaining the preference for crack nucleation at TBs.

3. Parent and twin pair crystallographic orientations with respect to remote loading direction were found to be very important in influencing TB slip activation and the elevation of local stored energy density and hence the likelihood of fatigue crack nucleation. The elastic anisotropy and resulting constraint affect the resolved shear stresses so that global Schmid factors are not necessarily good indicators of crack nucleation. Stored energy, which accounts for local stresses and strains provides better predictive capability. The simulations showed that the range of the most damaging parent grain orientation was over ~30^{o} about the grain <111> direction leading to the highest stored energy densities, and hence likelihood and preference for TB fatigue crack nucleation.

Declaration of Competing Interest

The authors declare that they have no known competing financial interests or personal relationships that could have appeared to influence the work reported in this paper.

Acknowledgements

Xiaoxian Zhang wishes to acknowledge the financial support provided by China Scholarship Council (CSC) and Fionn Dunne acknowledges with gratitude his Royal Academy of Engineering / Rolls-Royce research chair funding. This work is funded by the U.S. Dept. of Energy, Office of Basic Energy Sciences Program DE-SC0018901.

Appendix. 1

To examine the effect of the model (z-direction) thickness on free-surface results, a systematic analysis with different thicknesses (3μm, 6μm, 12μm) was conducted. Compared with the thickness of 3μm, higher thicknesses (two and four times this) show close results in strain distributions (Figure A1. (a)(b)(c)) and their magnitudes (Figure A1. (e)). Based on these results, it's reasonable to argue that the thickness effect is quite weak in this microstructure ROI, such that a thickness of 3μm is satisfactory.

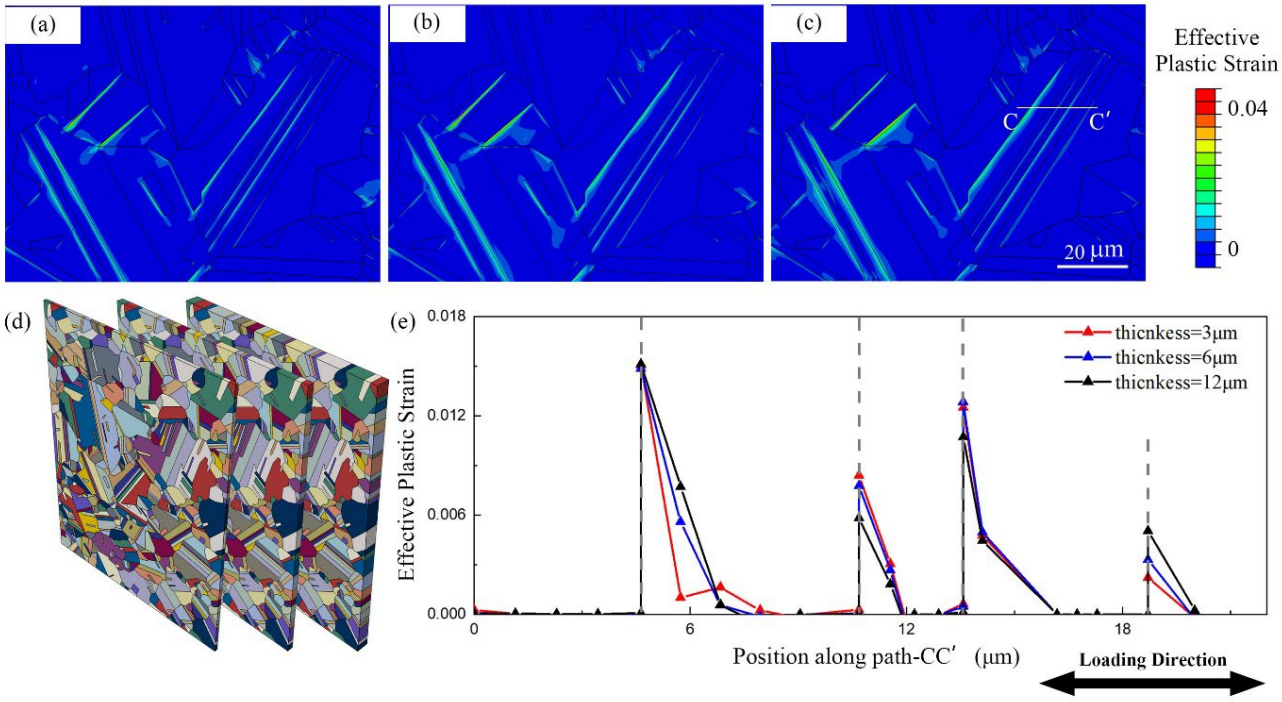

Figure A1 Effective plastic strain field after 1st cycle of the microstructure with (a) thickness=3μm, (b) thickness=6μm, (c) thickness=12μm. (d) Figures showing the microstructure with 3, 6, 12μm thickness and (e) Effective plastic strain along the path-CC' for the three thicknesses.

Appendix. 2

A statistical analysis based on the experimental data has been provided in [12] and provides the observational statistical link between the parallel slip at twins (with appropriate orientations) and the fatigue crack nucleation. In this study, we explicitly model two regions of the experimental microstructures which reproduce the conditions driving parallel slip and compare the results of the CP calculations with those obtained by averaging the DIC strain measurements. The comparisons are shown in Figure A2.

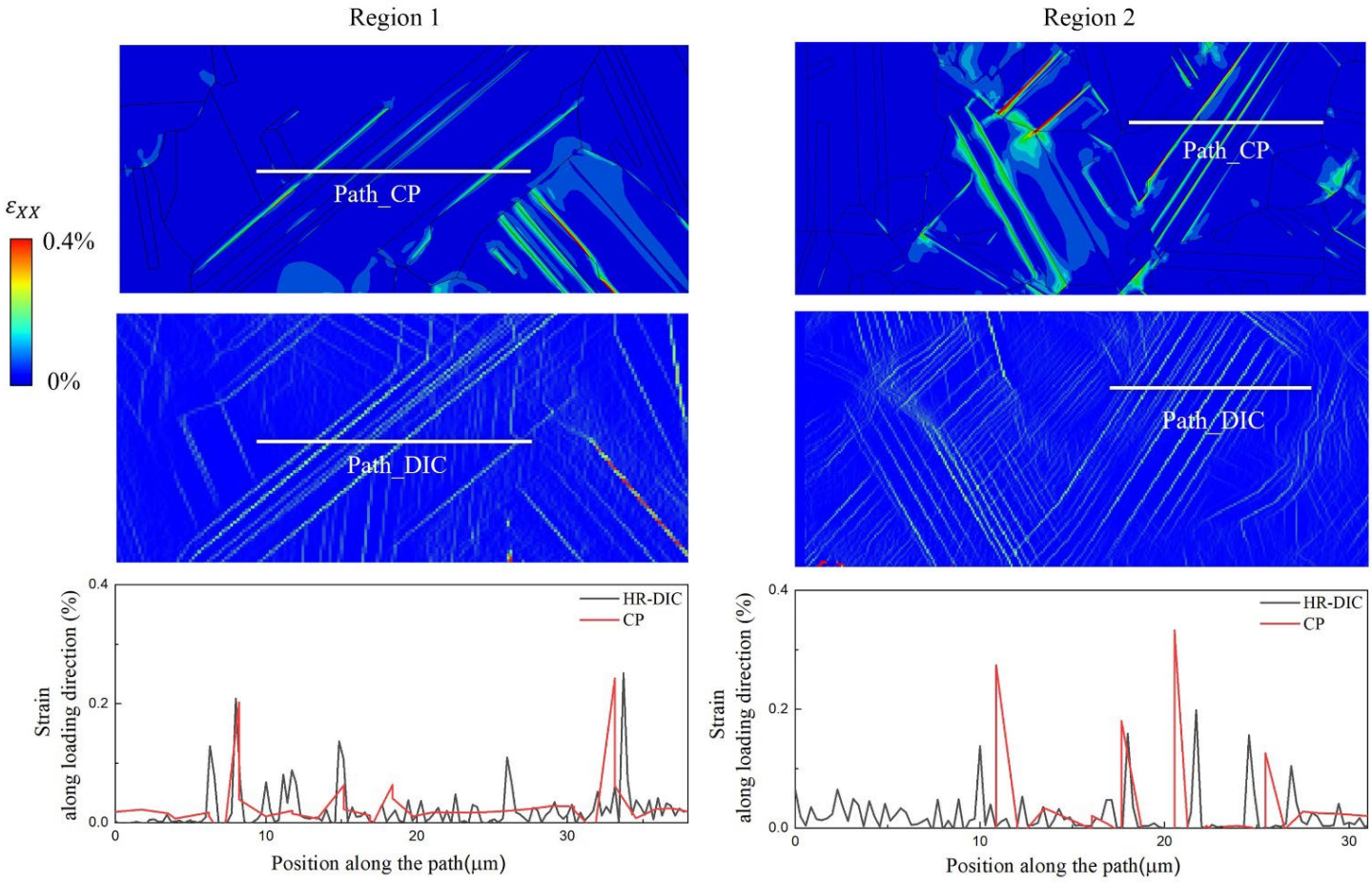

Figure A2. Contour plot distributions of DIC measured and CP calculated strains together with line graph comparisons of averaged DIC and CP calculated strains along the paths shown (along the loading direction) after the tensile phase of the 1st half cycle (unloaded).

References

[1] Sangid, M. D. (2013). The physics of fatigue crack initiation. International Journal of Fatigue, 57, 58–72. https://doi.org/10.1016/j.ijfatigue.2012.10.009

[2] Kubin, L., & Sauzay, M. (2016). Persistent slip bands: Similitude and its consequences. Acta Materialia, 104, 295–302. https://doi.org/10.1016/j.actamat.2015.11.010

[3] Kubin, L., & Sauzay, M. (2017). Persistent slip bands: The bowing and passing model revisited. Acta Materialia, 132, 517–524. https://doi.org/10.1016/j.actamat.2017.04.064

[4] Tanaka, K., & Mura, T. (1981). Dislocation Model for Fatigue Crack Initiation. American Society of Mechanical Engineers (Paper), 48(81-APM-3), 97–103.

[5] Mura, T. (1994). A theory of fatigue crack initiation. Materials Science and Engineering A, 176(1–2), 61–70. https://doi.org/10.1016/0921-5093(94)90959-8

[6] Chen, B., Jiang, J., & Dunne, F. P. E. (2018). Is stored energy density the primary meso-scale mechanistic driver for fatigue crack nucleation? International Journal of Plasticity, 101(December 2017), 213–229. https://doi.org/10.1016/j.ijplas.2017.11.005

[7] Wan, V. V. C., Maclachlan, D. W., & Dunne, F. P. E. (2014). A stored energy criterion for fatigue crack nucleation in polycrystals. International Journal of Fatigue, 68, 90–102. https://doi.org/10.1016/j.ijfatigue.2014.06.001

[8] Prastiti, N. G., Xu, Y., Balint, D. S., & Dunne, F. P. E. (2020). Discrete dislocation, crystal plasticity and experimental studies of fatigue crack nucleation in single-crystal nickel. International Journal of Plasticity, 126, 102615. https://doi.org/10.1016/j.ijplas.2019.10.003

[9] Heinz, A. and Neumann, P. (1990) 'Crack initiation during high cycle fatigue of an austenitic steel', Acta Metallurgica Et Materialia, 38(10), pp. 1933–1940. https://doi.org/10.1016/0956-7151(90)90305-z

[10] Stinville, J. C., Lenthe, W. C., Echlin, M. P., Callahan, P. G., Texier, D., & Pollock, T. M. (2017). Microstructural statistics for fatigue crack initiation in polycrystalline nickel-base superalloys. International Journal of Fracture, 208(1–2), 221–240. https://doi.org/10.1007/s10704-017-0241-z

[11] Stinville, J. C., Vanderesse, N., Bridier, F., Bocher, P., & Pollock, T. M. (2015). High resolution mapping of strain localization near twin boundaries in a nickel-based superalloy. Acta Materialia, 98, 29–42. https://doi.org/10.1016/j.actamat.2015.07.016

[12] Stinville, J. C., Lenthe, W. C., Miao, J., & Pollock, T. M. (2016). A combined grain scale elastic-plastic criterion for identification of fatigue crack initiation sites in a twin containing polycrystalline nickel-base superalloy. Acta Materialia, 103, 461–473. https://doi.org/10.1016/j.actamat.2015.09.050

[13] Stinville, J. C., Callahan, P. G., Charpagne, M. A., Echlin, M. P., Valle, V., & Pollock, T. M. (2020). Direct measurements of slip irreversibility in a nickel-based superalloy

using high resolution digital image correlation. Acta Materialia, 186, 172–189. https://doi.org/10.1016/j.actamat.2019.12.009

[14] Li, L. L., Zhang, Z. J., Zhang, P., Wang, Z. G., & Zhang, Z. F. (2014). Controllable fatigue cracking mechanisms of copper bicrystals with a coherent twin boundary. Nature Communications, 5. https://doi.org/10.1038/ncomms4536

[15] Li, L. L., Zhang, P., Zhang, Z. J., Zhou, H. F., Qu, S. X., Yang, J. B., & Zhang, Z. F. (2014). Strain localization and fatigue cracking behaviors of Cu bicrystal with an inclined twin boundary. Acta Materialia, 73, 167–176. https://doi.org/10.1016/j.actamat.2014.04.004

[16] Wei, D. A., Zaiser, M., Feng, Z., Kang, G., Fan, H., & Zhang, X. (2019). Effects of twin boundary orientation on plasticity of bicrystalline copper micropillars: A discrete dislocation dynamics simulation study. Acta Materialia, 176, 289–296. https://doi.org/10.1016/j.actamat.2019.07.007

[17] Sangid, M. D., Ezaz, T., Sehitoglu, H., & Robertson, I. M. (2011). Energy of slip transmission and nucleation at grain boundaries. Acta Materialia, 59(1), 283–296. https://doi.org/10.1016/j.actamat.2010.09.032

[18] Sangid, M. D., Maier, H. J., & Sehitoglu, H. (2011). The role of grain boundaries on fatigue crack initiation - An energy approach. International Journal of Plasticity, 27(5), 801–821. https://doi.org/10.1016/j.ijplas.2010.09.009

[19] Gustafson, S., Ludwig, W., Shade, P., Naragani, D., Pagan, D., Cook, P., … Sangid, M. D. (2020). Quantifying microscale drivers for fatigue failure via coupled synchrotron X-ray characterization and simulations. Nature Communications, 11(1), 1–10. https://doi.org/10.1038/s41467-020-16894-2

[20] Latypov, M. I., Stinville, J. C., Mayeur, J. R., Hestroffer, J. M., Pollock, T. M., & Beyerlein, I. J. (2021). Insight into microstructure-sensitive elastic strain concentrations from integrated computational modeling and digital image correlation. Scripta Materialia, 192, 78–82. https://doi.org/10.1016/j.scriptamat.2020.10.001

[21] Villechaise, P., Sabatier, L., & Girard, J. C. (2002). On slip band features and crack initiation in fatigued 316L austenitic stainless steel: Part 1: Analysis by electron back-scattered diffraction and atomic force microscopy. Materials Science and Engineering A, 323(1–2), 377–385. https://doi.org/10.1016/S0921-5093(01)01381-8

[22] Zhang, Z., Lunt, D., Abdolvand, H., Wilkinson, A. J., Preuss, M., & Dunne, F. P. E. (2018). Quantitative investigation of micro slip and localization in polycrystalline materials under uniaxial tension. International Journal of Plasticity, 108(April), 88–106. https://doi.org/10.1016/j.ijplas.2018.04.014

[23] Dunne, F. P. E., Rugg, D., & Walker, A. (2007). Lengthscale-dependent, elastically anisotropic, physically-based hcp crystal plasticity: Application to cold-dwell fatigue in Ti alloys. International Journal of Plasticity, 23(6), 1061–1083. https://doi.org/10.1016/j.ijplas.2006.10.013

[24] Dunne, F. P. E., Kiwanuka, R., & Wilkinson, A. J. (2012). Crystal plasticity analysis of micro-deformation, lattice rotation and geometrically necessary dislocation density. Proceedings of the Royal Society A: Mathematical, Physical and Engineering Sciences, 468(2145), 2509–2531.

https://doi.org/10.1098/rspa.2012.0050
[25] Cheng, J., & Ghosh, S. (2015). A crystal plasticity FE model for deformation with twin nucleation in magnesium alloys. International Journal of Plasticity, 67, 148–170. https://doi.org/10.1016/j.ijplas.2014.10.005
[26] Arsenlis, A., & Parks, D. M. (1999). Crystallographic aspects of geometrically-necessary and statistically-stored dislocation density. Acta Materialia, 47(5), 1597–1611. https://doi.org/10.1016/S1359-6454(99)00020-8
[27] Wan, V. V. C., Maclachlan, D. W., & Dunne, F. P. E. (2014). A stored energy criterion for fatigue crack nucleation in polycrystals. International Journal of Fatigue, 68, 90–102. https://doi.org/10.1016/j.ijfatigue.2014.06.001
[28] Chen, B., Jiang, J., & Dunne, F. P. E. (2017). Microstructurally-sensitive fatigue crack nucleation in Ni-based single and oligo crystals. Journal of the Mechanics and Physics of Solids, 106, 15–33. https://doi.org/10.1016/j.jmps.2017.05.012
[29] Zhang, T., Jiang, J., Britton, B., Shollock, B., & Dunne, F. (2016). Crack nucleation using combined crystal plasticity modelling, high-resolution digital image correlation and high-resolution electron backscatter diffraction in a superalloy containing non-metallic inclusions under fatigue. Proceedings of the Royal Society A: Mathematical, Physical and Engineering Sciences, 472(2189). https://doi.org/10.1098/rspa.2015.0792
[30] Du, X., & Zhao, J. C. (2018). First measurement of the full elastic constants of Ni-based superalloy René 88DT. Scripta Materialia, 152, 24–26. https://doi.org/10.1016/j.scriptamat.2018.03.044
[31] Frost, N. (1982). Reviews : Community Control of Social Services Departments (a discussion document) Peter and Suzie Beresford (1980) Available from Battersea Community Action, 27 Winders Rd., Battersea, London, SW1. 40p incl. p.&p. Critical Social Policy, 2(4), 113–114. https://doi.org/10.1177/026101838200200417
[32] Hull, Derek, and David J. Bacon. Introduction to dislocations. Butterworth-Heinemann, 2001.
[33] Sweeney, C. A., Vorster, W., Leen, S. B., Sakurada, E., McHugh, P. E., & Dunne, F. P. E. (2013). The role of elastic anisotropy, length scale and crystallographic slip in fatigue crack nucleation. Journal of the Mechanics and Physics of Solids, 61(5), 1224–1240. https://doi.org/10.1016/j.jmps.2013.01.001
[34] Echlin, J. C. S. M. P., Bridier, D. T. F., & Pollock, P. B. T. M. (2016). Sub-Grain Scale Digital Image Correlation by Electron Microscopy for Polycrystalline Materials during Elastic, 197–216. https://doi.org/10.1007/s11340-015-0083-4
[35] Miao, J., Pollock, T. M., & Wayne Jones, J. (2009). Crystallographic fatigue crack initiation in nickel-based superalloy René 88DT at elevated temperature. Acta Materialia, 57(20), 5964–5974. https://doi.org/10.1016/j.actamat.2009.08.022
[36] Michael D. Sangid, John Rotella, Diwakar Naragani, Jun-Sang Park, Peter Kenesei, Paul A. Shade, A complete grain-level assessment of the stress-strain evolution and associated deformation response in polycrystalline alloys, Acta Materialia, Volume 201, 2020, Pages 36-54, https://doi.org/10.1016/j.actamat.2020.09.051.
[37] Zheng, Z., Prastiti, N. G., Balint, D. S., & Dunne, F. P. E. (2019). The dislocation

configurational energy density in discrete dislocation plasticity. Journal of the Mechanics and Physics of Solids, 129, 39–60. https://doi.org/10.1016/j.jmps.2019.04.015

[38] Xu, Y., Wan, W. and Dunne, F. P. E. (2021) 'Microstructural fracture mechanics : Stored energy density at fatigue cracks', Journal of the Mechanics and Physics of Solids. Elsevier Ltd, 146(August 2020), p. 104209. https://doi: 10.1016/j.jmps.2020.104209.

[39] Lewis, A. C., Jordan, K. A., & Geltmacher, A. B. (2008). Determination of critical microstructural features in an austenitic stainless steel using image-based finite element modeling. Metallurgical and Materials Transactions A: Physical Metallurgy and Materials Science, 39 A(5), 1109–1117. https://doi.org/10.1007/s11661-008-9491-8

[40] Stein, C. A., Cerrone, A., Ozturk, T., Lee, S., Kenesei, P., Tucker, H., … Rollett, A. D. (2014). Fatigue crack initiation, slip localization and twin boundaries in a nickel-based superalloy. Current Opinion in Solid State and Materials Science, 18(4), 244–252. https://doi.org/10.1016/j.cossms.2014.06.001

[41] Zener C. Elasticity and anelasticity of metals[M]. University of Chicago press, 1948.

[42] Yeratapally, S. R., Glavicic, M. G., Hardy, M., & Sangid, M. D. (2016). Microstructure based fatigue life prediction framework for polycrystalline nickel-base superalloys with emphasis on the role played by twin boundaries in crack initiation. Acta Materialia, 107, 152–167. https://doi.org/10.1016/j.actamat.2016.01.038